

1 *This manuscript is a preprint and has been submitted to Geophysical Journal*
2 *International. It has undergone one round of peer-review. Subsequent*
3 *versions of this manuscript may have different content as a result of the*
4 *review process. If accepted, the final version of this manuscript will be*
5 *available via the 'Peer-reviewed Publication DOI' link on the right-hand side of*
6 *this webpage. We welcome feedback, so please feel free to contact any of the*
7 *authors directly or by leaving a comment.*

8

9

10

11 **Imaging evidence of subduction, collision, and** 12 **extension in northern Borneo: Constraints from** 13 **receiver functions** 14

15 Amy Gilligan(1),* David G. Cornwell(1), Nicholas Rawlinson(2), Felix Tongkul(3), Simone
16 Pilia(4), Tim Greenfield(2), Conor A. Bacon(5)

17

18

19

- 20 1. *School of Geosciences, University of Aberdeen, Aberdeen, UK*
- 21 2. *Department of Earth Sciences, University of Cambridge, Cambridge, UK*
- 22 3. *Faculty of Science and Natural Resources, Universiti Malaysia Sabah, Kota*
23 *Kinabalu, Malaysia*
- 24 4. *College of Petroleum Engineering and Geosciences, King Fahd University of*
25 *Petroleum and Minerals, Dhahran, Saudi Arabia*
- 26 5. *Lamont-Doherty Earth Observatory, Columbia University, Palisades, New York,*
27 *USA*

27 * *Corresponding author: amy.gilligan@abdn.ac.uk*

28

29

30 **Summary**

31

31 Northern Borneo (Sabah) has a complex geological history, having
32 experienced multiple episodes of subduction, magmatism, uplift, subsidence,
33 and extension since the Mesozoic. This includes the subduction of the proto-
34 South China Sea beneath what is now the north-western margin of Sabah,
35 which terminated ~21 Ma; a postulated later phase of northward subduction of
36 the Celebes Sea plate, which terminated ~9 Ma; extension in central Sabah
37 ~9-10Ma; rapid emplacement and exhumation of a granite intrusion ~7Ma,

38 which forms Mt Kinabalu today, and the development of a fold and thrust belt
39 offshore during the last 5 Myr. While these events have all left an imprint in
40 the rock record at the surface, it has not been possible, until recently, to
41 investigate deeper lithospheric processes that have shaped Sabah. However,
42 the installation of 46 broadband seismometers with a ~40 km station spacing
43 as part of the northern Borneo Orogeny Seismic Survey (nBOSS) between
44 2018 and 2020 means that for the first time it is now possible to constrain the
45 architecture of the crust and uppermost mantle beneath Sabah. Here we
46 present the results of receiver function analysis using two years of passive
47 seismic data recorded by the nBOSS network, and an additional 24 Malaysian
48 Meteorological Service broadband seismometers also located in Sabah. We
49 calculate P-wave receiver functions and use these in a joint inversion with
50 surface wave data to obtain shear velocity models of crustal structure. We find
51 that the crustal thickness in northern Borneo varies between 24 and 60 km.
52 The thickest crust occurs beneath the Crocker Range, while the thinnest crust
53 is found in central Sabah, potentially recording Miocene extension. The crust
54 beneath the 4095m high Mt Kinabalu is also comparatively thin. Distinct, low-
55 velocity, dipping anomalies identified in our shear wave velocity models
56 provide clear evidence for underthrusting of Dangerous Grounds continental
57 crust following subduction and collision.

58

59 **Keywords**

60

61 Asia; Crustal Structure; Crustal Imaging; Subduction Zone Processes; Joint
62 Inversion

63

64 **Introduction**

65

66 Subduction is fundamental to the growth of continents (e.g. Foley et al.,
67 2002), driving plate motion (Forsyth and Uyeda, 1975), and long-term climate
68 regulation (e.g. Johnston et al., 2011). Eventually subduction will come to an
69 end (e.g., via continent-continent collision), and this may result in magmatism,
70 exhumation, rapid uplift, and subsidence (e.g. Zandt et al., 2004, Levander et
71 al., 2011, Li et al., 2016). The processes occurring in these post-subduction
72 settings remain, at present, poorly understood. Given that subduction has
73 been happening on Earth for at least 1.8 Ga (Weller and St Onge, 2017),
74 explaining post-subduction processes is vital, not just for our understanding of
75 present-day tectonics, but also for interpreting the deep geological record.

76

77 Northern Borneo is an ideal location for studying post-subduction processes.
78 It is thought to be the site of two subduction systems that have terminated
79 since the start of the Neogene: the subduction of the proto-South China Sea
80 (pSCS) until ~21 Ma (Lai et al., 2021, Hall 2013, Morley and Back, 2008,
81 Tongkul 1994, Tongkul 1991) along the present-day NW coast of Sabah, and
82 the subduction of the Celebes Sea along the present-day SE coast of Sabah,
83 which terminated ~9 Ma (Lai et al., 2021). In this study we use passive
84 seismic data recorded by a network of broadband seismometers deployed
85 across the Malaysian state of Sabah, situated on the northern end of the
86 island of Borneo, between 2018-2020 (Figure 1) to image the crust and
87 mantle lithosphere to both improve our understanding of the tectonic setting of

88 northern Borneo and provide new insight into subduction termination and
89 post-subduction processes.

90

91 ***Geology and tectonic setting of Sabah***

92

93 The diverse surface geology of Sabah is testament to the rich range of
94 tectonic processes that have affected the northern part of Borneo since the
95 Mesozoic. The oldest dated rocks are those of the Segama Valley Felsic
96 Intrusions (250 and 241 Ma) (Burton-Johnson et al., 2020) in eastern Sabah,
97 which are intruded into ophitic rocks, with some subsequent, mineralogically
98 distinct, felsic intrusions in the same area being dated at ~178 Ma. It has been
99 proposed (Burton-Johnson et al. 2020, Balaguru and Nichols, 2004) that
100 these formed in an extensional basin in a suprasubduction setting, which was
101 then uplifted and eroded in the latest Cretaceous or earliest Paleocene,
102 around 66 Ma (Balaguru and Nichols, 2004).

103

104 By the Paleocene (66-56Ma) subduction of the proto-South China Sea
105 towards the south-east beneath what is now the western edge of Sabah had
106 begun (e.g., Hutchison et al., 2000, Rangin et al., 1999). Cumulate gabbros,
107 part of the Sabah Ophiolite, in the Tongod-Telupid area have been dated to
108 42.65 ± 0.51 Ma (Lai et al., 2021), and from their geochemical signature are
109 thought to have formed in a back-arc basin. Similarly, the geochemistry of the
110 Sandakan andesitic tuff (33.9 ± 7.7 Ma, Bergman et al., 2000) could also
111 suggest a back-arc basin setting (Lai et al., 2021, Hutchison et al., 2000). In
112 the fore-arc, thick (~9000 m) sedimentary successions of deep marine

113 sandstones, shales and minor conglomerates, are present in the NE-SW
114 trending Crocker Basin (Balaguru and Nichols, 2004).
115
116 Opening of the South China Sea (~33-32 Ma, (Franke, 2013, Barckhausen et
117 al., 2014, Li et al., 2014)), driven by subduction of the proto-South China Sea,
118 pushed continental slivers, including the Dangerous Grounds and Reed Bank
119 blocks, towards Borneo (e.g., Tongkul 1991, Tongkul 1994, Hutchison et al.,
120 2000, Hall 2013, Rangin et al., 1999). Subduction of the proto-South China
121 Sea continued in the earliest part of the Miocene (24-21 Ma, Lai et al., 2021
122 and references therein), however, at around 21 Ma the Dangerous Grounds
123 block collided with and then underthrust northern Borneo (Lai et al., 2021, Hall
124 2013, Morley and Back, 2008, Tongkul 1994, Tongkul 1991), which ultimately
125 caused subduction to cease. This collision led to uplift above sea level
126 (Burton-Johnson et al, 2020, Hall 2013, Morley and Back, 2008). However, by
127 the end of the Early Miocene, most of Sabah was at or below sea level once
128 more, with low hills where the Crocker Range is today (Hall 2013, Cottam et
129 al, 2013).
130
131 Subduction of the Celebes Sea beneath eastern Sabah began at a similar
132 time to the termination of subduction of the proto-South China Sea and may
133 have been a result of changes in regional stresses due to the Sabah-
134 Dangerous Grounds collision (Lai et al., 2021, Linang et al., 2022). In the Dent
135 Peninsular, rocks that are the product of arc magmatism have been dated to
136 18.8-17.8 Ma and in the Semporna Peninsula to 18.2-14.4 Ma (Macpherson
137 et al., 2010). It is, however, important to note that the idea that there was

138 northwards subduction of the Celebes Sea is contested (Burton-Johnson and
139 Cullen, 2023). A slab from this subduction event has yet to be imaged in the
140 mantle.

141

142 Roll-back of the Celebes Sea subduction from 19 Ma led to extension in the
143 Sulu Sea and in Sabah (Hall, 2013). Thick (~6 km) successions of
144 carbonates, shallow marine, and fluvio-deltaic sediments, including coals,
145 were deposited in a basin in Central Sabah (Tongkul and Chang, 2003,
146 Balaguru and Nichols 2004, Burton-Johnson et al., 2021). The coastal/shelf
147 environments for all these sediments, including coal that was buried to 3 km
148 depth (Baluguru and Nichols, 2004), means that subsidence must have
149 continued over a prolonged period. Tsikouras et al., (2021) argue that the
150 major increase in extension suggested by Huang (1991) between 9 and 11
151 Ma led to rifting in Ranau area, and suggest that sea-floor spreading took
152 place in the Telupid area. This is disputed by Cullen and Burton-Johnson
153 (2021) who argue that while extension took place, the Sulu Sea rift did not
154 extend into Sabah. In a recent review Lai et al., (2021) suggest that Celebes
155 Sea subduction beneath Borneo terminated ~9 Ma.

156

157 The Kinabalu pluton, which forms the 4095 m high Mt Kinabalu, was intruded
158 into peridotites and the Crocker formation between 7.85 and 7.22 Ma, at a
159 depth of 3-8 km (Cottam et al., 2013). Between 6.6 and 5.8 Ma it was rapidly
160 cooled and exhumed with rates of up to 7 mm/yr (Cottam et al., 2013). The
161 emplacement and exhumation of the Kinabalu pluton likely occurred in an
162 extensional setting (Hall et al., 2013, Burton-Johnson et al., 2019).

163

164 Sabah only became fully emergent above sea level by the end of the Miocene
165 to early Pliocene (~5 Ma), and uplift has occurred since (Roberts et al., 2018,
166 Hall 2013, Morley and Black 2008). This includes uplift of the circular basins,
167 such as the Maliau Basin, in central Sabah (Tongkul and Chang, 2003).
168 During the Pliocene large-scale gravitational collapse occurred, seen in mass
169 transport slumps, megaslides and extensional faults (Cottam et al., 2013), and
170 as result of this, a fold and thrust belt has developed offshore of western
171 Sabah (e.g., Spain et al., 2013, Franke et al., 2008, King et al., 2010). Around
172 5 Ma a change in the composition of volcanic rocks in eastern Sabah also
173 occurs from calc-alkaline to a similar composition to ocean island basalts
174 (OIB), (Macpherson et al., 2010). Volcanism in eastern Sabah has continued
175 into the Holocene, potentially as recently as 24-27 ka based on radiocarbon
176 dating of carbonised material (Kirk, 1968; Bellwood, 1988; cited in Tjia et al.,
177 1992), although Takashima et al., (2004) date the youngest volcanics in their
178 study using thermo-luminescence to 90 ka.

179

180 ***Previous geophysical work***

181

182 Regional-scale tomographic studies of South-East Asia have observed
183 anomalously high seismic velocities in the upper mantle beneath Sabah at
184 depths of ~100-300 km (e.g., Amaru, 2007, Tang and Zheng, 2013, Hall and
185 Spakman, 2015, Zenonos et al., 2019, Wehner et al., 2022). These high
186 velocities are attributed to the presence of slab remnants in the upper mantle.
187 While the earlier body-wave studies (e.g., Amaru, 2007, Hall and Spakman

188 2015, Zenonos et al., 2019) had limited resolution beneath Sabah, thus
189 bringing the existence of higher velocities into question, the full-waveform
190 model of Wehner et al., (2022), SASSY21, uses data from the same dense
191 seismic network in Borneo used in this study, and so has improved resolution
192 in this region. Other results from this dense seismic network – the nBOSS
193 network – are described below.

194

195 In a Sabah-focused P- and S-wave tomographic study, also using nBOSS
196 data, Pilia et al., (2023a), observe two distinct fast velocity anomalies in the
197 upper mantle beneath Sabah. One, an elongate anomaly at depths >250 km
198 underlying most of the Crocker Range, is attributed to the proto-South China
199 Sea Slab, while the other, a relatively narrow (<100 km) anomaly between
200 ~150 and 300 km depth in central Sabah, is interpreted to be a lithospheric
201 drip from the volcanic arc root beneath the Semporna Peninsular. Pilia et al.,
202 (2023b) perform thermo-mechanical modelling and suggest that the
203 downwelling drip can cause extension and crustal thinning, resulting in
204 melting and exhumation of sub continental material. As such, the ‘Semporna
205 drip’ may play an important role in the emplacement of the Kinabalu pluton, as
206 well as explaining subsidence and uplift, and the lavas with an OIB
207 composition in eastern Sabah.

208

209 Bacon et al., (2022) investigate anisotropy beneath Sabah using XKS splitting
210 measurements extracted from nBOSS teleseismic data. Their results
211 demonstrate that fossil anisotropy in the lithosphere is the main control on
212 anisotropic properties in this post-subduction setting. They observe fast

213 directions parallel to the strike of the Crocker range in western Sabah, likely
214 imparted when the Dangerous Grounds block collided with Sabah. In the east
215 of Sabah, fast directions are sub-parallel to the direction of spreading in the
216 Sulu Sea, suggesting that the anisotropic fabric may have developed as a
217 result of extension, while the null results they observe in the southeast may
218 arise due to the lithospheric drip observed by Pilia et al., (2023a).

219

220 Roberts et al., (2018) suggest that removal of the lithosphere and
221 replacement by hot asthenospheric material could explain the relatively rapid
222 uplift and erosion rates observed in Sabah (~0.1-0.3 mm/yr, Morely and Back,
223 2008). They base their estimates of thin lithosphere on regionally extensive
224 slow shear wave velocities at 100-200 km depth in the global tomographic
225 model of Schaeffer and Lebedev (2014). However, in recent 2-plane-wave
226 tomography of Sabah from Greenfield et al., (2022), average lithosphere
227 thickness beneath Sabah is found to be ~100 km, with the lithosphere only
228 being thin (<50km) beneath the Semporna Peninsula, consistent with the work
229 of Pilia et al., (2023b) that suggests that the lithosphere here has dripped off.

230

231 Until recently, estimates of crustal thickness in Sabah had been limited. Holt
232 (1998) modelled gravity data from Sabah and suggested that the whole of
233 Sabah was underlain by crust >30 km thick, that crustal thicknesses beneath
234 the Crocker Range were ~50 km, and 39 km beneath central Sabah.

235 Estimates of 27 ± 3 km and 33 ± 2 km beneath seismometers KKM and LDM
236 near Kota Kinabalu and Lahad Datu respectively have been made by Lipke
237 (2008) from H-k stacking of receiver functions. A regional crustal thickness

238 map derived from surface wave data made by Tang and Zheng (2013)
239 estimates crustal thickness beneath Sabah to be 27.5-32.5 km. The
240 deployment of the nBOSS seismic network between 2018-2020 has allowed
241 for more detailed studies of crustal thickness to be conducted. Greenfield et
242 al. (2022) use the 4.1 km/s velocity contour in their shear wave velocity model
243 as a proxy for the Moho and suggest that crustal thicknesses vary from 25-55
244 km, with the thickest crust beneath the Crocker Range and the Dent
245 Peninsula, and the thinnest crust in north east Sabah. Linang et al. (2022) use
246 Virtual Deep Seismic Sounding (VDSS) to estimate crustal thickness in the
247 range 21 - 46 km, with a similar pattern of thicker and thinner crust.

248

249 Until now, due to a lack of seismic instrumentation in the region, it has not
250 been possible to derive a detailed model of the seismic velocity structure of
251 Sabah's crust. Consequently, debates have continued to emerge (e.g.,
252 Milsom et al. 2001, Cullen and Burton-Johnson, 2021) about the nature of the
253 crust beneath this part of Borneo and the processes that have shaped it.

254

255 In this study, we calculate radial P-wave receiver functions at 70 seismic
256 stations, including the recent nBOSS deployment across Sabah, and jointly
257 invert these with surface wave data to develop the first detailed shear velocity
258 model of the crust in Sabah, allowing us to map the Moho geometry beneath.
259 These results provide important constraints on processes that have shaped
260 the region.

261

262 **Data and Methods**

263

264 Broadband teleseismic data in this study come from two seismic networks
265 deployed in Sabah (Figure 1, Supplementary Table 1). The temporary nBOSS
266 network of 46 seismometers, installed mostly on a ~40x40 km grid , with a
267 mean interstation distance of 37.5km (Bacon, 2021), between March 2018
268 and January 2020, consisted of 18 Güralp 3ESPD instruments and 28 Güralp
269 6TD instruments (Rawlinson, 2018, Pilia et al., 2019). We also used data from
270 the Malaysian Metrological Service permanent seismic network. In Sabah, this
271 consists of 24 permanently installed Streckeisen STS2/2.5 and SS1-Ranger
272 seismometers, predominantly located in regions of elevated seismicity around
273 Mt Kinabalu and Darvel Bay.

274

275 Calculation of radial P receiver functions from 3-component seismograms of
276 teleseismic (30-90° epicentral distance) earthquakes allows us to investigate
277 the structure of the crust, including determining Moho depth and identifying
278 layering within the crust.

279

280 We performed the initial quality control of the seismograms in two stages.
281 First, a total of 27,660 3-component seismograms from March 2018-
282 September 2018 for earthquakes $M_w > 5$ that met the distance criteria were
283 visually inspected. Where the P-wave signal-to-noise ratio was high (e.g., a P
284 arrival could clearly be identified) on all 3 components, these seismograms
285 were classified as 'good' and were taken forward for further analysis. All other
286 seismograms were rejected and classified as 'bad'. Using this classified data
287 set we developed a deep learning algorithm to determine the probability of a
288 3-component seismogram being suitable for further analysis. The annotated

289 (good or bad) seismograms were converted into spectrograms and 80% of the
290 data were used to train an image classification convolutional neural network,
291 ResNet50, pretrained on ImageNet (He et al., 2016). The data classification
292 algorithm was then tested using the remaining 20 per cent of the data and had
293 a 92.7 per cent accuracy. A total of 57,858 3-component seismograms from
294 September 2018-January 2020 were then used with the classification
295 algorithm, and only those classified with a greater than 50 per cent probability
296 of being 'good' were visually inspected. This significantly reduced the time
297 needed for this stage of data quality control, while resulting in a similar
298 proportion of events being taken forward for further analysis.

299

300 After initial quality control, 14,447 seismograms were used to calculate
301 receiver functions using the time-domain iterative deconvolution method of
302 Ligorria and Ammon (1999), with a gaussian width of 1.6, corresponding to a
303 frequency of 0.9Hz. Further quality control steps included removal of receiver
304 functions with a poor fit (<70 per cent), and those which appeared noisy,
305 oscillatory or anomalous to other receiver functions from a similar distance
306 and backazimuth on visual inspection. This left a remaining dataset of 3338
307 receiver functions. Eight stations, one from the nBOSS network, and seven
308 from the Malaysian Metrological Service permanent seismic network, had no
309 usable receiver functions. For stations with usable receiver functions, the
310 number of receiver functions at individual seismometers ranges from 9 at
311 SPM to 183 at SBA8 (Supplementary Table 1, Supplementary Figure 1). This
312 is due to variations in the amount of data available from individual stations
313 and the noise levels at the installation sites.

314

315 Receiver functions at an individual station are stacked together to reduce
316 noise, and these stacks are used in an inversion for crustal velocity structure.
317 While useful, the interpretation of receiver functions on their own is inherently
318 non-unique (Ammon et al., 1990). Therefore, to ensure that shear velocities
319 we obtain from inversions of receiver functions are realistic for this region, we
320 jointly invert the receiver functions with fundamental mode Rayleigh wave
321 group velocity dispersion curves extracted from the GDM52 global compilation
322 (Ekström, 2011) for each station location for a period range 25–250 s. This
323 model is relatively coarse ($1^\circ \times 1^\circ$), does not see much variation in group
324 velocities beneath Sabah (Supplementary Figure 2), and with a minimum
325 period of 25s, is most sensitive to depths of 25km and below, corresponding
326 to the mid to lower crust and upper mantle in this area. We are primarily
327 concerned in this study that the inversions result in velocity models that fit the
328 receiver function data.

329

330 The radial P receiver function stacks, together with the dispersion curves, for
331 each station were inverted for shear velocity structure using joint96
332 (Herrmann, 2013), an iterative linearised least squares inversion method.
333 Several starting models were tested including constant values of 4.48 km/s,
334 (mantle velocity in the ak135 model - see Kennett et al., 1995), 4.28 km/s, and
335 3.70 km/s and a V_p/V_s value of 1.74 down to 100 km depth, parameterised
336 into 2 km thick layers, overlying ak135. While there are some small variations
337 in the absolute shear velocities due to differences in the starting models, they
338 are sufficiently small to not alter the interpretation of the structure. We test

339 different relative weights (p value in joint96) of surface waves to receiver
340 function data in the inversion: 0.5, 0.1, 0.05 and 0.01. Models with $p=0.5$ are
341 smoother than those with a lower p value, reflecting the greater contribution of
342 surface wave data. Overall, the models show little variation in structure with p
343 value, indicating that the recovered features are robust (Supplementary
344 Figure 3).

345 In order to test the stability of the results, the receiver functions at each station
346 were divided into 3 time periods (March 2018-Sept 2018, Sept 2018-March
347 2019, March 2019-Jan 2020) and were stacked and inverted separately.

348 There was very little difference between the resulting models and those
349 obtained from the complete dataset (Supplementary Figure 4). This can be
350 considered a form of bootstrapping, and gives us further confidence that the
351 results are robust

352 **Results**

353

354 *Individual receiver functions*

355 Plotting individual receiver functions with respect to backazimuth (e.g
356 Supplementary Figure 1, Supplementary Figure 5), shows that for some
357 stations there is a degree of variability for events at different backazimuths.
358 There are a number of potential causes of this, including short-length scale
359 variation in crustal structure, anisotropy in the crust, and dipping layers in the
360 crust. Unfortunately the backazimuthal range of events in this study is limited,
361 with events being mainly to the north east or south east of the seismometers,
362 meaning it is not possible to model the cause of the backazimuthal variation

363 effectively. Because of this limitation, we consider all receiver functions at a
364 station in a signal stack.

365

366 At some stations we observe receiver functions that do not fit with the typical
367 idea of a receiver function, which in some automated QC approaches would
368 have been rejected. One of the most extreme examples of this are the
369 receiver functions computed for events recorded by the station SBG3
370 (Supplementary Figure 5). Here, the amplitude of the first arrival is relatively
371 low, merging with a large amplitude positive arrival at ~2. There is a large
372 amplitude negative arrival at ~4s, and a large amplitude positive arrival at ~5s.
373 At this station there are 52 individual receiver functions that have this pattern
374 (i.e all those with north easterly or south easterly backazimuths). Further, the
375 Malaysian Metrological Service seismometer PTM, located ~20km from
376 SBG3, also shows similar pattern of positive and negative arrivals. PTM is a
377 different type of seismometer, deployed in a different way to SBG3. The
378 consistency between multiple events, and similarities between receiver
379 functions at different, but relatively close, locations suggests that, while these
380 receiver functions are not necessarily typical, they do reflect real crustal
381 structure.

382

383 *Stacked receiver functions*

384

385 Stacked receiver functions at each station are plotted on cross-sections
386 across Sabah (Figure 2). Cross-section A (Figure 2 (a)) cuts through the
387 highest topography in Sabah in the region around Mt Kinabalu. Heading SE

388 from the NW coast there is a positive arrival that decreases from ~4.5 s to ~3
389 s delay time at the stations immediately beneath the highest topography.
390 Moving further SE, the delay time of this prominent positive arrival then
391 increases to ~7 s at station SBE4 (dark grey dashed line). At stations to the
392 SE of Mt Kinabalu, this positive arrival is preceded by a large amplitude
393 negative arrival that similarly shows an increase in arrival time from ~3 s at
394 SBF2 to ~5 s at SBE4 (light grey dashed line). There is a clear change in the
395 character of the receiver functions from ~200 km along the cross section, with
396 the portion of cross-section A between SBD5 and SBD7 having a large
397 amplitude positive arrival at ~6-6.5 s (dark grey dashed line).

398

399 In cross-section B (Figure 2 (b)), the stations in the Crocker Range have a
400 relatively consistent large amplitude positive arrival (dark grey dashed line) at
401 ~4 s, while at SBB3 and SBD4, immediately to the SE, the largest amplitude
402 positive arrival appears to be at ~6.5 s. Between these stations and those in
403 the vicinity of the Maliau Basin there is a strong positive arrival at ~3.5 s, while
404 at the stations near to the Maliau Basin there is an arrival at ~5 s. At the
405 south-east end of the cross-section, in the Semporna Peninsula, the largest
406 positive arrivals, after the direct P arrival, is again at a shorter delay time of
407 around 4 s.

408

409 The peak at ~0 s should correspond to the direct P arrival; however if there
410 are low-velocity sediments in the uppermost crust the P-to-S conversion from
411 the base of these may interfere with the direct P resulting in the first positive
412 arrival being shifted away from 0 s. This is observed at several sites,

413 e.g., SBD6 (Figure 2 (a)) and MALB (Figure 2 (b)) and is anticipated given the
414 thick sedimentary basins (>6 km sediments, Hall, 2013) in Sabah.

415

416 *Shear velocity structure*

417

418 Using the 1-D shear wave velocity model beneath each station, 2D,
419 composite velocity cross sections have been constructed using bicubic
420 interpolation for several lines across Sabah. The models shown in Figure 3
421 are derived from the inversions that used $p=0.1$ and the 3.7 km/s starting
422 model; however, the features remain consistent with the various weightings
423 and starting models tested. Given the high weight of the receiver functions in
424 the models shown, the descriptions and interpretations of the models are
425 primarily concerned with changes in velocity, and relative velocities, rather
426 than absolute velocities. The orientations of cross-sections A and B are
427 chosen to be approximately perpendicular to the strike of the Crocker range,
428 while cross-sections C, D, and E are chosen to help further elucidate the 3D
429 crustal structure.

430 In cross-section A (Figure 3(a)), low velocity sedimentary basins, labelled as 1
431 in the cross-section, are illuminated offshore to the NW (SBG1) and in the
432 south-eastern half of the cross-section (SE of SBE4), confirming the
433 observation of a broadened, delayed P arrival in the receiver function stacks.
434 Low velocities extend to depths of ~10 km. The most striking feature of this
435 cross-section is a dipping high velocity layer, labelled 2, extending from SBE3
436 to SBE5 from ~5 km to 50 km depth, with a dip in the cross section to the SE,
437 which overlies a low velocity layer, labelled 3, with a similar dip. This fits the

438 pattern of arrivals seen in the receiver function cross-sections: a seemingly
439 dipping transition from a high velocity to a low velocity layer resulting in a
440 negative arrival, followed by a low to high velocity discontinuity with increasing
441 depth.

442 In cross-section B (Figure 3(b)) low velocities, labelled 4, are also observed to
443 ~10 km depth in the vicinity of known sedimentary basins between SBC4 and
444 SBA7. The transition to mantle velocities ($\sim >4.2$ km/s in this model) occurs at
445 ~30-35 km depth in the north-western part of the cross section but deepens to
446 greater than 40 km beneath SBC4. It shallows to ~25 km beneath SBB4 and
447 SBC5, before deepening to ~35 km again beneath the Maliau Basin. This
448 agrees with the pattern of positive arrivals observed in the stacked receiver
449 functions, with those for stations between the Crocker Range and the Maliau
450 Basin experiencing the shortest delay times. At the southeast end of cross-
451 section B, the crust beneath SBA8 and SBA9 has lower velocities (~ 3.9 km/s
452 in this model) at the gradient interpreted to be the Moho, labelled 5, than
453 beneath stations elsewhere in the section.

454

455 The differences in crustal structure from south to north through western
456 Sabah is highlighted in cross-section C (Figure 3(c)). The crustal structure at
457 the north-east end of this section, to the north of Mt Kinabalu, has a different
458 character to that in the central portion of the section (between SBD2 and
459 SBE3). In the north east, very high velocities (>4.2 km/s in this model),
460 labelled 6, are observed at ~20 km, while in the central portion they are
461 generally low (<3.4 km/s in this model) at this depth in a somewhat
462 discontinuous layer, labelled 7, likely the dipping low velocity layer observed

463 in cross-section A. Cross-section D (Figure 3(d)) cuts to the east of the
464 Crocker Range, through the Maliau Basin. In the south west of this section
465 there is a northeasterly dipping transition from crust to mantle velocities (~4.2
466 km/s in this model) from 25 to 45 km depth between SBA3 and the Maliau
467 Basin. At SBC5 it decreases sharply to a depth of 25 km, the depth it is also
468 observed to be at between SBE4 and SBF4. Beneath SBD4 relatively high
469 velocities are observed in the upper crust, labelled 8, and low velocities are
470 observed between 25 and 45km depth. This location corresponds with where
471 ophitic material is found on the surface around Telupid (e.g. Hall 2013) . In the
472 south of cross-section E (Figure 3(e)), which cuts through the Semporna and
473 Dent Peninsulas, the transition between crustal and mantle velocities at ~35
474 km depth is relatively gradual. This contrasts with further north, where this
475 transition is sharper, and upper mantle velocities are faster.

476

477 *Moho depth*

478

479 The depth of the Moho beneath each station is picked from its corresponding
480 1-D shear velocity model at the depth that corresponds to the base of the
481 steepest positive velocity gradient where shear velocity exceeds 4 km/s
482 (Figure 4). The depth of the Moho is found to vary from 24 km at SBC6 and
483 SBF4 to 60 km at MTM, although most other measurements are <48 km. The
484 deepest Moho is found in a SW-NE trending band on the eastern edge of the
485 Crocker Range, where the Moho depth exceeds 40 km. It is also relatively
486 deep (40-44 km) beneath the Maliau Basin and beneath other circular basins
487 to the north of the Maliau Basin, and to the west of the Segama ophiolite. The

488 shallowest Moho depth (24-26 km) is found in a band between the Crocker
489 Range and the circular basins, with changes in Moho depth of ~15-25 km
490 occurring over short lateral distances (~20 km).

491

492 At the stations marked with white hexagons in Figure 4, it was not clear where
493 the Moho should be picked. For instance, at a subset of stations (e.g., SBD6,
494 SBD7, and SBC8) there is a very gradual increase in velocities over a wide
495 (~40 km) depth range (Supplementary Figure 6), while at other stations (e.g.,
496 SBD5, SBE4, and SBG3) the models have two steep velocity gradients, both
497 of which could represent plausible Moho locations given those found
498 elsewhere in Sabah, for example at 28km and 58km for SBD5.

499

500 **Discussion**

501

502 *Limitations of the models*

503

504 The 1D velocity models obtained in the study have a number of limitations,
505 which should be acknowledged in order to avoid over interpretation of the
506 results. The receiver functions used in the inversions are single stacks for
507 each station. This is done to reduce noise and source effects, however it may
508 mask real complexity in crustal structure such as short-length scale lateral
509 variations, anisotropy and dipping layers, which we have not be able to model
510 due to the limitations imposed by the backazimuthal range of the events.

511 Therefore it is likely that crustal structure beneath Sabah is more complex

512 than shown in the models here.

513

514 In the inversions we use the relatively coarse, global model, GDM52
515 (Ekstrom, 2011), to help ensure the shear velocities are reasonable for the
516 regional context. While the fits to the dispersion curves are reasonably good
517 (Supplementary Figure 3), the focus of this study is the constraints provided
518 by the radial P wave receiver functions, and so we prioritise the fit to the
519 receiver functions for the models that we interpret. As the models are strongly
520 weighted to the receiver functions, this means that the best constrained
521 features in the crustal structure will be the velocity discontinuities, such as the
522 Moho, rather than absolute velocities.

523

524 *Processes affecting crustal thickness*

525

526 It is important to account for the effect of the interference between
527 conversions and multiples (e.g., Gilligan et al., 2014): a consequence is that
528 the largest signal on a receiver function should not necessarily be interpreted
529 as being due to the velocity increase at the Moho. However, there is a
530 consistent pattern between the positive arrivals observed in the stacked
531 receiver functions and the velocity changes at the Moho observed in the
532 models from joint inversion, suggesting that the receiver functions can, in this
533 instance, provide an interpretable picture for trends in Moho depth.

534

535 The variations in crustal thickness across Sabah observed in this study are in
536 general agreement with the estimates made by recent studies using 2-plane-
537 wave tomography (Greenfield et al., 2022) and virtual deep seismic sounding
538 (Linang et al., 2022): central Sabah appears to have significantly thinner crust

539 than that beneath the Crocker Range and the Circular Basins (Supplementary
540 Figure 7). One notable difference with the Greenfield et al., (2022) Moho
541 estimate is beneath the Semporna Peninsular they observe thick crust
542 (>55km), while in this study we observe crustal thickness of ~34km. This
543 difference is likely to arise due to Greenfield et al., (2022) using the 4.1km/s
544 shear velocity contour as a proxy for Moho depth, and this, as discussed
545 below, may not be an appropriate velocity proxy for the lower crust/upper
546 mantle beneath the Semporna Peninsular.

547

548 The pattern of thicker and thinner crust broadly agrees with the estimates of
549 Holt (1998) using gravity data; however, between the Crocker Range and
550 thickened crust beneath the circular basins we observe a significantly thinner
551 crust (e.g., 25 and 24 km at SBC5 and SBC6 respectively) than the 32 km
552 suggested by Holt (1998). Modelling gravity data is notoriously non-unique,
553 and Holt (1998) uses a very simple model for crustal densities. Given the lack
554 of other constraints on the properties of the crust at the time this may have
555 been appropriate; however, the lateral and vertical heterogeneity of the crust
556 demonstrated in this study indicates a more complex model is required, which
557 may alter the estimates of crustal thickness from the gravity data.

558

559 It should be noted that the crust in this study is thicker throughout much of
560 Sabah than was shown in interpretative cross-section of Hall (2013), which
561 bases Moho depth off the results of Holt (1998), modified for denser material.
562 Hall (2013)'s cross-section shows a maximum Moho depth of 40 km beneath
563 the Crocker Range, and around 20 km beneath both the circular basins and

564 the Dent and Semporna peninsulas. Further, our estimates of crustal
565 thickness shows a significantly different pattern and depths to the estimates
566 made by Tang and Zheng (2013). They report crustal thicknesses of ~27.5 to
567 32.5 km, increasing southward across Sabah, based on the depth of the 4
568 km/s velocity contour in their shear velocity model. This model encompasses
569 the whole of the South China Sea and surrounding region and, as such, has
570 more limited resolution in Sabah compared to this study and others
571 (Greenfield et al., 2022, Linang et al., 2022) that have used the data from the
572 nBOSS network. The thicker crust we observe, compared to earlier estimates,
573 may mean that there is a larger contribution from regional tectonic shortening
574 to the regional uplift observed by Roberts et al., (2018).

575

576 The relatively thick crust (>40 km) beneath the Crocker Range, particularly on
577 the eastern side, is likely to have been thickened during the Sabah Orogeny
578 (~23 Ma), when the Dangerous Grounds block collided with the western edge
579 of northern Borneo at the final stage of the subduction of the proto-South
580 China Sea (e.g., Hutchison et al., 2000, Hall 2013, Rangin et al., 1999). The
581 velocity discontinuity picked as the Moho for many stations in the Crocker
582 Range is the base of the SE dipping slow velocities seen in cross-section A,
583 which we interpret as the base of the underthrust Dangerous Grounds crust.

584

585 Extension, related to the roll-back of the Celebes Sea slab (e.g., Hall, 2013),
586 could have thinned the crust in central Sabah to 20-25 km. Indeed, Tsikouras
587 et al. (2021) argue that the basalts they date to 9-10 Ma in the Telupid area,
588 are rift-related, thus implying significant extension and crustal thinning,
589 although this is disputed by Cullen and Burton-Johnson (2021). A double

590 discontinuity is observed in our study in the 1-D velocity models at some
591 stations (e.g., SBE4), and could indicate that it may not necessarily be
592 appropriate to simply interpret the velocity gradient at ~20-25 km as a single
593 Moho. If the crust is 20-25 km thick, the question as to the extent to which this
594 crust may have been thinned remains, i.e., what was the pre-extensional
595 crustal thickness? Greenfield et al. (2022) assume that it was 40-50 km, as is
596 observed beneath the Crocker Range and circular basins, and thus calculate
597 a stretching factor of 1.3-2. However, if this area was not significantly
598 thickened during the Sabah Orogeny, which is plausible given the lack of
599 underthrust Dangerous Grounds material observed in this study, then pre-
600 extensional thickness may have been less to begin with.

601

602 Related to the question of pre-extensional thickness is whether the ~45 km
603 thick crust observed beneath the Maliau Basin and other circular basins is a
604 result of thickening during the Sabah orogeny (~23 Ma). After thickening it
605 may have been separated from other thickened crust beneath the Crocker
606 Range as a result of extension (e.g., in a crustal scale boudinage process as
607 suggested by Linang et al. (2022)). Alternatively, the crust may have been
608 thickened at a later point in time. Tongkul and Chang (2003) suggest that
609 eastern Sabah experienced N-S compression in the mid Middle Miocene (~13
610 Ma), which led to the segmentation of the large basin in eastern Sabah that
611 had been active in the Early Miocene, and NW-SE compression in the late
612 Upper Miocene (~7-5 Ma), which enhanced the circular shape of the basins,
613 with a period of sediment deposition in between these two compressional
614 events. It may be that during these compressional episodes, potentially

615 associated with Celebes Sea subduction, some crustal thickening occurred
616 beneath the circular basins.
617
618 While areas of the highest topography may be anticipated to have some of the
619 thickest crust, intriguingly beneath the stations in the vicinity of the 4095m
620 high Mt Kinabalu the crust is only 30-35km thick. The Kinabalu Granite was
621 emplaced between 7.2-7.8Ma (Cottam et al., 2013), well after the termination
622 proto-South China Sea subduction, thus it would be expected that the crust in
623 this region would have been thickened as a result of this collision. The
624 thermomechanical modelling of Pilia et al., (2023b) shows that as a result of a
625 downwelling drip, e.g the Semporna drip, a region of initially thick crust can be
626 thinned. This thinning could facilitate melting of the lower crust, thus it may be
627 that both the presence of the Kinabalu pluton and the thinner-than-anticipated
628 crust we observe can both be explained by part of the lithosphere having
629 dripped off beneath the Semporna peninsula.

630

631 *Crustal structure*

632

633 Given the diversity of the surface geology in Sabah, it is unsurprising that the
634 crust shows considerable variation. The key elements of our interpretation are
635 shown in Figure 5.

636

637 We interpret the low velocity (<3.4 km/s in our model) layer seen dipping to
638 the south east from the west coast of Sabah to the eastern edge of the
639 Crocker Range in Cross-section A (Figure 3(a)) as Dangerous Grounds

640 material that has been underthrust beneath Sabah. Underthrusting of
641 attenuated Dangerous Grounds crust has been proposed as the mechanism
642 by which subduction of the proto-SCS stopped (e.g., Hall, 2013, Morley and
643 Back, 2008, Hutchison, 2000), but this is arguably the first time it has been
644 imaged. Cross-section B (Figure 3(b)), which cuts to the south of Cross-
645 section A, also has a low velocity layer at depths of 20-25 km. In this instance
646 this layer does not seem to dip. We consider this to also be underthrust
647 Dangerous Grounds crust, although this suggests potential along strike
648 variation in the nature of the collision between Sabah and the Dangerous
649 Grounds. Rangin et al. (1999), considering the whole of the proto-SCS, argue
650 that the proto-SCS basin was narrower off the coast of Borneo than the Sulu
651 Sea, and it may be that the differences we observe in underthrust Dangerous
652 Grounds crust are a manifestation of this. Furthermore, Greenfield et al.,
653 (2022) note that the lithosphere is thinner in the southwest of Sabah, again
654 suggesting that different processes may have influenced this area compared
655 to those further north.

656

657 Overlying the low-velocity layer in Cross-section A is a high velocity layer,
658 also dipping to the south east, with velocities exceeding 4 km/s in our model
659 in what is interpreted as the upper- to mid-crust. The velocities we observe
660 are consistent with this being mafic to ultramafic material, although, as noted
661 above, the velocities in our models should primarily be interpreted relatively
662 due to the high weight of receiver function observations in the inversion.
663 However, as this high velocity layer appears to lie beneath areas of peridotitic
664 rocks near Ranau and ophiolitic rocks near Telupi, we interpret the layer as

665 obducted ophitic material. It is not possible to constrain the timing of the
666 emplacement from this study, e.g., it may be the result of late Mesozoic rifting
667 (Tsikouras et al., 2021), or it could have been emplaced earlier (e.g., Cullen
668 and Burton-Johnson 2021).

669

670 The crustal structure of the northern tip of Sabah (to the north of SBF2) is
671 distinct from areas to the south, as is particularly seen in Cross-section C
672 (Figure 3(c)), suggesting that distinct geological processes have shaped this
673 region. The change in the character of the crustal structure is in the same
674 place where there is a change in strike of the surface geology, from ~SW-NE
675 to the south to ~WNW-ESE in the north (Tongkul 1990), in the vicinity of Mt
676 Kinabalu. Moreover, it is approximately coincident with where the fast velocity
677 anomaly in the upper mantle that Pilia et al. (2023a) associate with the proto-
678 South China Sea slab terminates. Tongkul (1994) suggests, based on the
679 relationships between sedimentary rocks in this region, that the basement
680 here - Mesozoic oceanic crust - is uplifted relative to the area to the south.
681 Tongkul (1994) further suggests that this region was affected by the collision
682 with the Reed Bank, resulting in N-S compression, while further south the
683 collision was with the Dangerous Grounds block. Gozzard et al., (2018)
684 observe that the crust beneath the Reed Bank has not been thinned in the
685 same way as the Dangerous Grounds block. Franke et al., (2008) also note
686 the presence of the Kudat block off the eastern shore of northernmost Sabah,
687 which active source seismic data suggests has a different crustal structure. It
688 may be that the different properties of blocks colliding with Sabah, as well as
689 the orientation of the collisions, resulted in the contrasting crustal structure we

690 observe today: underthrust material to the south but not at the northern tip of
691 Sabah.

692

693 In the east of Sabah, the lower crust and upper mantle beneath stations in the
694 Semporna Peninsula (SBA8 and SBA9) is relatively slow (~3.8-4 km/s for the
695 uppermost mantle compared to 4.3-4.5 km/s elsewhere). This is similar to the
696 results from the two-plane wave tomography of Greenfield et al. (2022).

697 Volcanism in this area occurred until at least 0.2 Ma (Lai et al., 2021) and
698 potentially as recently as 24-27 ka (Kirk, 1968; Bellwood, 1988; cited in Tjia et
699 al., 1992) with hot springs found in the vicinity of Tawau today, with water
700 temperatures of up to 75°C (Siong et al., 1991). Pilia et al. (2023b) and
701 Greenfield et al. (2022) propose that part of the lithosphere has been removed
702 beneath the Semporna Peninsula and has been replaced by hot
703 asthenospheric material. This would mean that the remaining crust and
704 mantle would be expected to be warm and thus seismically slow, as we
705 observe here.

706

707

708

709 **Conclusion**

710

711 We present a high-resolution crustal shear velocity model of Sabah, northern
712 Borneo, from the joint inversion of P receiver functions and surface wave
713 data. We image, for the first time, Dangerous Grounds crust underthrust
714 beneath most of the Crocker Range. This has had the effect of thickening the

715 crust beneath the present-day mountain range, with crustal thicknesses
716 exceeding 40 km. However, beneath Mt Kinabalu, crustal thicknesses are
717 only in the range 30-35km, supporting earlier ideas (Cottam et al., 2013,
718 Sapin et al., 2013, Tsikouras et al., 2021, Pilia et al., 2023b) that some degree
719 of crustal thinning may have been involved in its emplacement. Thinner crust
720 (~25 km) between the Crocker Range and the Circular Basins may be due to
721 extension related to the rollback of the Celebes Sea slab (Hall, 2013),
722 although the amount of extension remains unclear given that pre-extensional
723 crustal thickness remains unknown. Thicker crust (>40 km) beneath the
724 Maliau and other circular basins suggests that these areas have experienced
725 some degree of crustal thickening, which given the late-mid Miocene age of
726 the sediments that have been deformed is likely to have occurred later than
727 the ~21 Ma Sabah Orogeny. Relatively slow velocities in the lower crust and
728 upper mantle beneath the Semporna Peninsula support work by Pilia et al.
729 (2023b) and Greenfield et al. (2021) that lithospheric delamination has
730 occurred here.

731

732 Overall, we observe a high degree of heterogeneity in the crustal structure
733 beneath Sabah, on length scales of 10s of kilometres. This highlights the
734 complexity of subduction, collisional, post-subduction, and extensional
735 processes that have shaped Sabah over the Cenozoic, and reinforces the
736 importance of dense instrumentation in order to better understand tectonic
737 activity that has occurred in similar settings.

738

739 **Acknowledgements**

740 Thanks to all those who were involved in the deployment, servicing and
741 recovery of the nBOSS network between March 2018 and January 2020.
742 Many thanks to the landowners throughout Sabah who hosted seismometers.
743 Seismometers used in the nBOSS network were provided by the University of
744 Cambridge, the University of Aberdeen (Aberdeen University Geophysical
745 Equipment Repository – AUGER), and the Natural Environment Research
746 Council (NERC) Geophysical Equipment Facility through SeisUK (loan 1038).
747 We thank MetMalaysia for providing access to their restricted continuous
748 waveform data recorded by their permanent MY network in Sabah. A.G was
749 supported by a Royal Astronomical Society Independent Research
750 Fellowship. S. P was supported by the Natural Environmental Research
751 Council (NERC) Grant NE/R013500/1 and from the European Union's Horizon
752 2020 Research and Innovation Program under Marie Skłodowska-Curie Grant
753 Agreement 790203. T.G. was supported by an Early Career Fellowship from
754 the Leverhulme Trust. We have made use of several open source Python
755 packages in our analysis and visualisation, including Matplotlib (Hunter,
756 2007); and ObsPy (Beyreuther et al., 2010). A number of figures were
757 produced using the Generic Mapping Tools version 6 (Wessel et al.,
758 2019). We thank Robert Herrmann for making the Computer Programs in
759 Seismology freely available. We thank two anonymous reviewers and the
760 editor Gabi Laske for constructive comments, which have helped clarify the
761 focus of the paper.

762

763

764 **Data availability**

765

766 The nBOSS dataset is accessible through the EarthScope Data Management

767 Center (https://www.fdsn.org/networks/detail/YC_2018/). Data from the

768 Malaysian national seismic network

769 (<https://www.fdsn.org/networks/detail/MY/>) are restricted but may be obtained

770 by contacting the Malaysian Meteorological Department. The exceptions to

771 this are stations KKM and LDM which are also available through the

772 Earthscope Data Management Center. The Open Science Framework site for

773 this project, which includes figures for each station analysed can be found at:

774 <https://osf.io/2zvcg/>

775

776 **Author contributions**

777

778 **A.G.:** Formal analysis, conceptualisation, funding acquisition, investigation,

779 resources, visualisation, writing – original draft; **D.C.:** Investigation, resources,

780 writing - review and editing; **N.R.:** Conceptualisation, funding acquisition,

781 resources, investigation, writing – review and editing; **F.T.:** Conceptualisation,

782 resources, investigation; **S.P.:** Investigation, writing – review and editing,

783 funding acquisition; **T.G.:** Investigation, writing – review and editing; **C.B.:**

784 Data curation, investigation.

785

786

787

788

789

790

791

792

793 **References**

794

795 Amaru, M. L. (2007). *Global travel time tomography with 3-D reference models* (Vol. 274).
796 Utrecht University.
797

798 Ammon, C. J., Randall, G. E., & Zandt, G. (1990). On the nonuniqueness of receiver function
799 inversions. *Journal of Geophysical Research: Solid Earth*, 95(B10), 15303-15318.
800

801 Bacon, C. A. (2021). *Seismic anisotropy and microseismicity: from crustal formation to*
802 *subduction termination*, University of Cambridge (United Kingdom)
803

804

805 Bacon, C. A., Rawlinson, N., Pilia, S., Gilligan, A., Wehner, D., Cornwell, D. G., & Tongkul, F.
806 (2022). The Signature of Lithospheric Anisotropy at Post-Subduction Continental Margins:
807 New Insight From XKS Splitting Analysis in Northern Borneo. *Geochemistry, Geophysics,*
808 *Geosystems*, 23(11), e2022GC010564.
809

810 Balaguru, A., & Nichols, G. (2004). Tertiary stratigraphy and basin evolution, southern Sabah
811 (Malaysian Borneo). *Journal of Asian Earth Sciences*, 23(4), 537-554.
812

813 Barckhausen, U., Engels, M., Franke, D., Ladage, S., & Pubellier, M. (2014). Evolution of the
814 South China Sea: Revised ages for breakup and seafloor spreading. *Marine and Petroleum*
815 *Geology*, 58, 599-611.
816

817 Bellwood, P. S. (1988). Archaeological research in south-eastern Sabah. Sabah Museum and
818 State Archives
819

820 Beyreuther, M., Barsch, R., Krischer, L., Megies, T., Behr, Y., & Wassermann, J. (2010).
821 ObsPy: A Python toolbox for seismology. *Seismological Research Letters*, 81(3), 530-533.
822

823 Bird, P. (2003). An updated digital model of plate boundaries. *Geochemistry, Geophysics,*
824 *Geosystems*, 4(3).
825

826 Burton-Johnson, A., Macpherson, C. G., Muraszko, J. R., Harrison, R. J., & Jordan, T. A.
827 (2019). Tectonic strain recorded by magnetic fabrics (AMS) in plutons, including Mt Kinabalu,
828 Borneo: A tool to explore past tectonic regimes and syn-magmatic deformation. *Journal of*
829 *Structural Geology*, 119, 50-60.
830

831 Burton-Johnson, A., Macpherson, C. G., Millar, I. L., Whitehouse, M. J., Ottley, C. J., &
832 Nowell, G. M. (2020). A Triassic to Jurassic arc in north Borneo: Geochronology,
833 geochemistry, and genesis of the Segama Valley Felsic Intrusions and the Sabah
834 ophiolite. *Gondwana Research*, 84, 229-244.
835

836 Burton-Johnson, A., & Cullen, A. B. (2023). Continental rifting in the South China Sea through
837 extension and high heat flow: An extended history. *Gondwana Research*, 120, 235-263
838
839

840 Cottam, M. A., Hall, R., Sperber, C., Kohn, B. P., Forster, M. A., & Batt, G. E. (2013).
841 Neogene rock uplift and erosion in northern Borneo: evidence from the Kinabalu granite,
842 Mount Kinabalu. *Journal of the Geological Society*, 170(5), 805-816.
843

844 Cullen, A., & Burton-Johnson, A. (2021). [Comment] New zircon radiometric U-Pb ages and
845 Lu-Hf isotopic data from the ultramafic-mafic sequences of Ranau and Telupid (Sabah,
846 eastern Malaysia): Time to reconsider the geological evolution of Southeast
847 Asia?. *Geology*, 49(11), 541-541.
848

849 Forsyth, D., & Uyeda, S. (1975). On the relative importance of the driving forces of plate
850 motion. *Geophysical Journal International*, 43(1), 163-200.
851

852 Franke, D., Barckhausen, U., Heyde, I., Tingay, M., & Ramli, N. (2008). Seismic images of a
853 collision zone offshore NW Sabah/Borneo. *Marine and Petroleum Geology*, 25(7), 606-624.
854

855 Ekström, G. (2011). A global model of Love and Rayleigh surface wave dispersion and
856 anisotropy, 25-250 s. *Geophysical Journal International*, 187(3), 1668-1686.
857

858 Foley, S., Tiepolo, M., & Vannucci, R. (2002). Growth of early continental crust controlled by
859 melting of amphibolite in subduction zones. *Nature*, 417(6891), 837-840.
860

861 Franke, D. (2013). Rifting, lithosphere breakup and volcanism: Comparison of magma-poor
862 and volcanic rifted margins. *Marine and Petroleum geology*, 43, 63-87.
863

864 Gilligan, A., Roecker, S. W., Priestley, K. F., & Nunn, C. (2014). Shear velocity model for the
865 Kyrgyz Tien Shan from joint inversion of receiver function and surface wave
866 data. *Geophysical Journal International*, 199(1), 480-498.
867

868 Gozzard, S., Kuszniir, N., Franke, D., Cullen, A., Reemst, P., & Henstra, G. (2019). South
869 China Sea crustal thickness and oceanic lithosphere distribution from satellite gravity
870 inversion. *Petroleum Geoscience*, 25(1), 112-128.
871

872 Greenfield, T., Gilligan, A., Pilia, S., Cornwell, D. G., Tongkul, F., Widiyantoro, S., &
873 Rawlinson, N. (2022). Post-Subduction Tectonics of Sabah, Northern Borneo, Inferred From
874 Surface Wave Tomography. *Geophysical Research Letters*, 49(3), e2021GL096117.
875

876 Hall, R. (2013). Contraction and extension in northern Borneo driven by subduction
877 rollback. *Journal of Asian Earth Sciences*, 76, 399-411.
878

879 Hall, R., & Spakman, W. (2015). Mantle structure and tectonic history of SE
880 Asia. *Tectonophysics*, 658, 14-45.
881

882 He, K., Zhang, X., Ren, S., & Sun, J. (2016). Deep residual learning for image recognition.
883 In *Proceedings of the IEEE conference on computer vision and pattern recognition* (pp. 770-
884 778).
885

886 Herrmann, R. B. (2013). Computer programs in seismology: An evolving tool for instruction
887 and research. *Seismological Research Letters*, 84(6), 1081-1088.
888

889 Hunter, J. D. (2007). Matplotlib: A 2D graphics environment. *Computing in science &*
890 *engineering*, 9(03), 90-95.
891

892 Hutchison, C. S., Bergman, S. C., Swauger, D. A., & Graves, J. E. (2000). A Miocene
893 collisional belt in north Borneo: uplift mechanism and isostatic adjustment quantified by
894 thermochronology. *Journal of the Geological Society*, 157(4), 783-793.
895

896 Holt, R. A. (1998). *The gravity field of Sundaland-acquisition, assessment and interpretation*.
897 University of London, University College London (United Kingdom)
898

899 Huang, Z., Gradstein, F.M., and Loudon, K.E., (1991). Subsidence and sedimentation
900 analysis of marginal basins: Celebes Sea and Sulu Sea, Leg 124, Sites 767 and 768,
901 in Silver, E.A., Rangin, C., von Braymann, M.T., et al, Proceedings of the Ocean Drilling
902 Program, *Scientific Results*, 124, 399-407
903

904 Johnston, F. K., Turchyn, A. V., & Edmonds, M. (2011). Decarbonation efficiency in
905 subduction zones: Implications for warm Cretaceous climates. *Earth and Planetary Science*
906 *Letters*, 303(1-2), 143-152.
907

908 Kennett, B. L., Engdahl, E. R., & Buland, R. (1995). Constraints on seismic velocities in the
909 Earth from traveltimes. *Geophysical Journal International*, 122(1), 108-124.
910

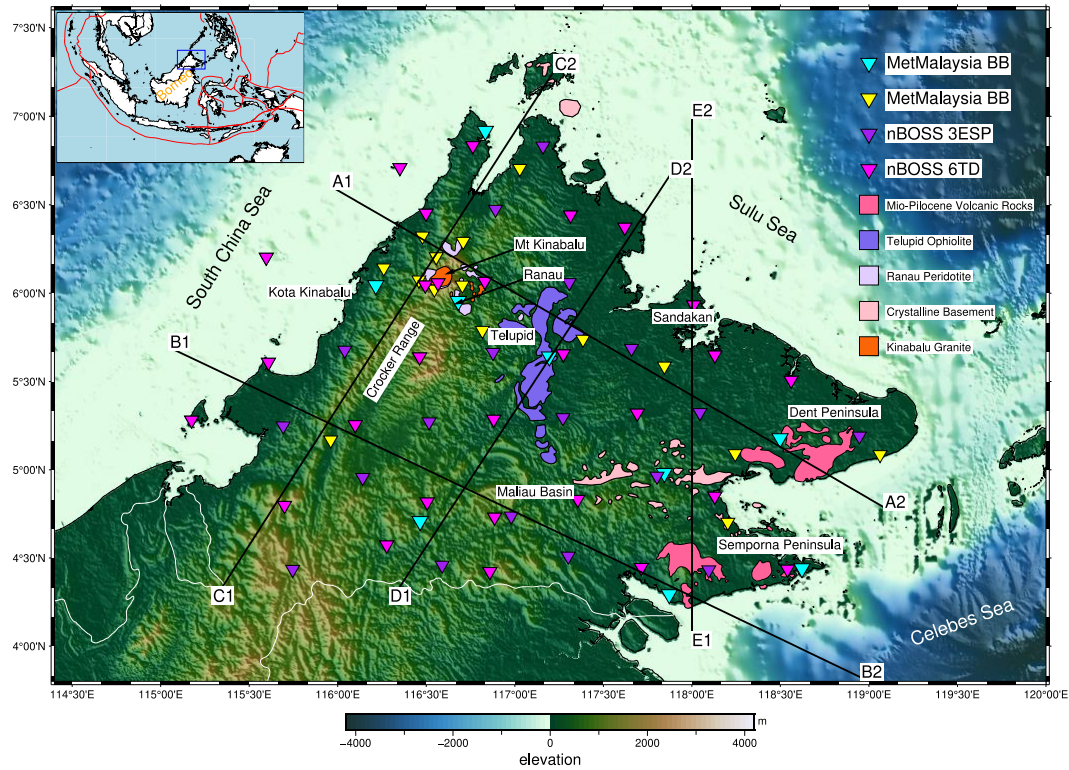
911 Kirk, H. J. C. (1968). The igneous rocks of the Sarawak and Sabah. *Geological Survey*
912 *Borneo Region, Malaysia, Bull*, 5, 201.
913
914

915 Lai, C. K., Xia, X. P., Hall, R., Meffre, S., Tsikouras, B., Rosana Balangué-Tarriela, M. I., ... &
916 Norazme, N. A. (2021). Cenozoic Evolution of the Sulu Sea Arc-Basin System: An
917 Overview. *Tectonics*, 40(2), e2020TC006630.
918
919 Levander, A., Schmandt, B., Miller, M. S., Liu, K., Karlstrom, K. E., Crow, R. S., Lee, C.-T. A.,
920 & Humphreys, E. D. (2011). Continuing Colorado plateau uplift by delamination-style
921 convective lithospheric downwelling. *Nature*, 472(7344), 461-465.
922
923 Li, C. F., Xu, X., Lin, J., Sun, Z., Zhu, J., Yao, Y., ... & Zhang, G. L. (2014). Ages and
924 magnetic structures of the South China Sea constrained by deep tow magnetic surveys and
925 IODP Expedition 349. *Geochemistry, Geophysics, Geosystems*, 15(12), 4958-4983.
926
927 Li, Z. H., Liu, M., & Gerya, T. (2016). Lithosphere delamination in continental collisional
928 orogens: A systematic numerical study. *Journal of Geophysical Research: Solid
929 Earth*, 121(7), 5186-5211.
930
931 Ligorria, J. P., & Ammon, C. J. (1999). Iterative deconvolution and receiver-function
932 estimation. *Bulletin of the seismological Society of America*, 89(5), 1395-1400.
933
934 Linang, H. T., Pilia, S., Rawlinson, N., Bacon, C. A., Gilligan, A., Cornwell, D. G., & Tongkul,
935 F. (2022). Collision-induced subduction polarity reversal explains the crustal structure of
936 northern Borneo: New results from Virtual Deep Seismic Sounding (VDSS). *Geophysical
937 Research Letters*, 49(19), e2022GL099123.
938
939 Lipke, K. (2008). Seismologic investigation of the Sunda arc region with receiver
940 functions. *Potsdam: University of Potsdam*.
941
942 Macpherson, C. G., Chiang, K. K., Hall, R., Nowell, G. M., Castillo, P. R., & Thirlwall, M. F.
943 (2010). Plio-Pleistocene intra-plate magmatism from the southern Sulu Arc, Semporna
944 peninsula, Sabah, Borneo: Implications for high-Nb basalt in subduction zones. *Journal of
945 Volcanology and Geothermal Research*, 190(1-2), 25-38.
946
947 Milsom, J., Holt, R., Hutchison, C. S., Bergman, S. C., Swauger, D. A., & Graves, J. E.
948 (2001). Discussion of a Miocene collisional belt in north Borneo: uplift mechanism and
949 isostatic adjustment quantified by thermochronology: *Journal*, Vol. 157, 2000, 783–
950 793. *Journal of the Geological Society*, 158(2), 396-400.
951
952 Morley, C. K., & Back, S. (2008). Estimating hinterland exhumation from late orogenic basin
953 volume, NW Borneo. *Journal of the Geological Society*, 165(1), 353-366.
954
955 Pilia, S., Rawlinson, N., Gilligan, A., & Tongkul, F. (2019). Deciphering the fate of plunging
956 tectonic plates in Borneo. *Eos, Transactions American Geophysical Union*, 100(10), 18-23.
957
958 Pilia, S., Rawlinson, N., Hall, R., Cornwell, D. G., Gilligan, A., & Tongkul, F. (2023a). Seismic
959 signature of subduction termination from teleseismic P-and S-wave arrival-time tomography:
960 The case of northern Borneo. *Gondwana Research*, 115, 57-70.
961
962 Pilia, S., Davies, D. R., Hall, R., Bacon, C. A., Gilligan, A., Greenfield, T., Tongkul, F., Kramer,
963 S. C., Wilson, C. R., Ghelichkhan, S., Cornwell, D. G., Colli, L., & Rawlinson, N. (2023b).
964 Post-subduction tectonics induced by extension from a lithospheric drip. *Nature Geoscience*,
965 1-7. Rangin, C., Spakman, W., Pubellier, M., & Bijwaard, H. (1999). Tomographic and
966 geological constraints on subduction along the eastern Sundaland continental margin (South-
967 East Asia). *Bulletin de la Société géologique de France*, 170(6), 775-788.
968
969 Rawlinson, N. (2018). *Northern Borneo Orogeny Seismic Survey* [Data set]. International
970 Federation of Digital Seismograph Networks. https://doi.org/10.7914/SN/YC_2018
971
972 Roberts, G. G., White, N., Hoggard, M. J., Ball, P. W., & Meenan, C. (2018). A Neogene
973 history of mantle convective support beneath Borneo. *Earth and Planetary Science
974 Letters*, 496, 142-158.

- 975
976 Sapin, F., Hermawan, I., Pubellier, M., Vigny, C., & Ringenbach, J. C. (2013). The recent
977 convergence on the NW Borneo Wedge—a crustal-scale gravity gliding evidenced from
978 GPS. *Geophysical Journal International*, 193(2), 549-556.
979
980 Schaeffer, A. J., & Lebedev, S. (2013). Global shear speed structure of the upper mantle and
981 transition zone. *Geophysical Journal International*, 194(1), 417-449.
982
983 Siong, L. P., Intang, F., & On, C. F. (1991). Geothermal prospecting in the Semporna
984 Peninsula with emphasis on the Tawau area. *Geological Society of Malaysia, Bulletin 29*,
985 135-155
986
987 Takashima I., Nazri, A. A., Lim, P. S., Koseki, T., Mouri, Y., Nasution, A., & Sucipta, I. E.,
988 (2004). Thermoluminescence age determination of quaternary volcanic rocks and alteration
989 products at Tawau area, Sabah, Malaysia. *Journal of the Geothermal Research Society of*
990 *Japan*, 26(3), 273-283.
991
992
993 Tang, Q., & Zheng, C. (2013). Crust and upper mantle structure and its tectonic implications
994 in the South China Sea and adjacent regions. *Journal of Asian Earth Sciences*, 62, 510-525.
995 Tjia, H. D., Komoo, I., Ali, C. A., & Tahir, S. H. (1992). Geology of Taman Bukit Tawau,
996 Semporna Peninsula, Sabah. *Geological Society of Malaysia, Bulletin 31*, 113-131
997
998 Tongkul, F. (1990). Structural style and tectonics of Western and Northern Sabah. *Geological*
999 *Society of Malaysia, Bulletin 27*, 227-239
1000
1001 Tongkul, F. (1991). Tectonic evolution of Sabah, Malaysia. *Journal of Southeast Asian Earth*
1002 *Sciences*, 6(3-4), 395-405.
1003
1004 Tongkul, F. (1994). The geology of Northern Sabah, Malaysia: its relationship to the opening
1005 of the South China Sea Basin. *Tectonophysics*, 235(1-2), 131-147.
1006
1007 Tongkul, F., and Chang, F. K. (2003) Structural geology of the Neogene Maliau Basin, Sabah.
1008 *Geological Society of Malaysia, Bulletin 47*, 51-61
1009
1010 Tsikouras, B., Lai, C. K., Ifandi, E., Teo, C. H., & Xia, X. P. (2021). New zircon radiometric U-
1011 Pb ages and Lu-Hf isotopic data from the ultramafic-mafic sequences of Ranau and Telupid
1012 (Sabah, eastern Malaysia): Time to reconsider the geological evolution of Southeast
1013 Asia?. *Geology*, 49(7), 789-793.
1014
1015 Wehner, D., Blom, N., Rawlinson, N., Böhm, C., Miller, M. S., Suspendi, P., & Widiyantoro, S.
1016 (2022). SASSY21: A 3-D Seismic Structural Model of the Lithosphere and Underlying Mantle
1017 Beneath Southeast Asia From Multi-Scale Adjoint Waveform Tomography. *Journal of*
1018 *Geophysical Research: Solid Earth*, 127(3), e2021JB022930.
1019
1020 Wessel, P., Luis, J. F., Uieda, L., Scharroo, R., Wobbe, F., Smith, W. H., & Tian, D. (2019).
1021 The generic mapping tools version 6. *Geochemistry, Geophysics, Geosystems*, 20(11), 5556-
1022 5564.
1023
1024 Zandt, G., Gilbert, H., Owens, T. J., Ducea, M., Saleeby, J., & Jones, C. H. (2004). Active
1025 foundering of a continental arc root beneath the southern Sierra Nevada in
1026 California. *Nature*, 431(7004), 41-46.
1027
1028 Zenonos, A., De Siena, L., Widiyantoro, S., & Rawlinson, N. (2019). P and S wave travel time
1029 tomography of the SE Asia-Australia collision zone. *Physics of the Earth and Planetary*
1030 *Interiors*, 293, 106267.
1031

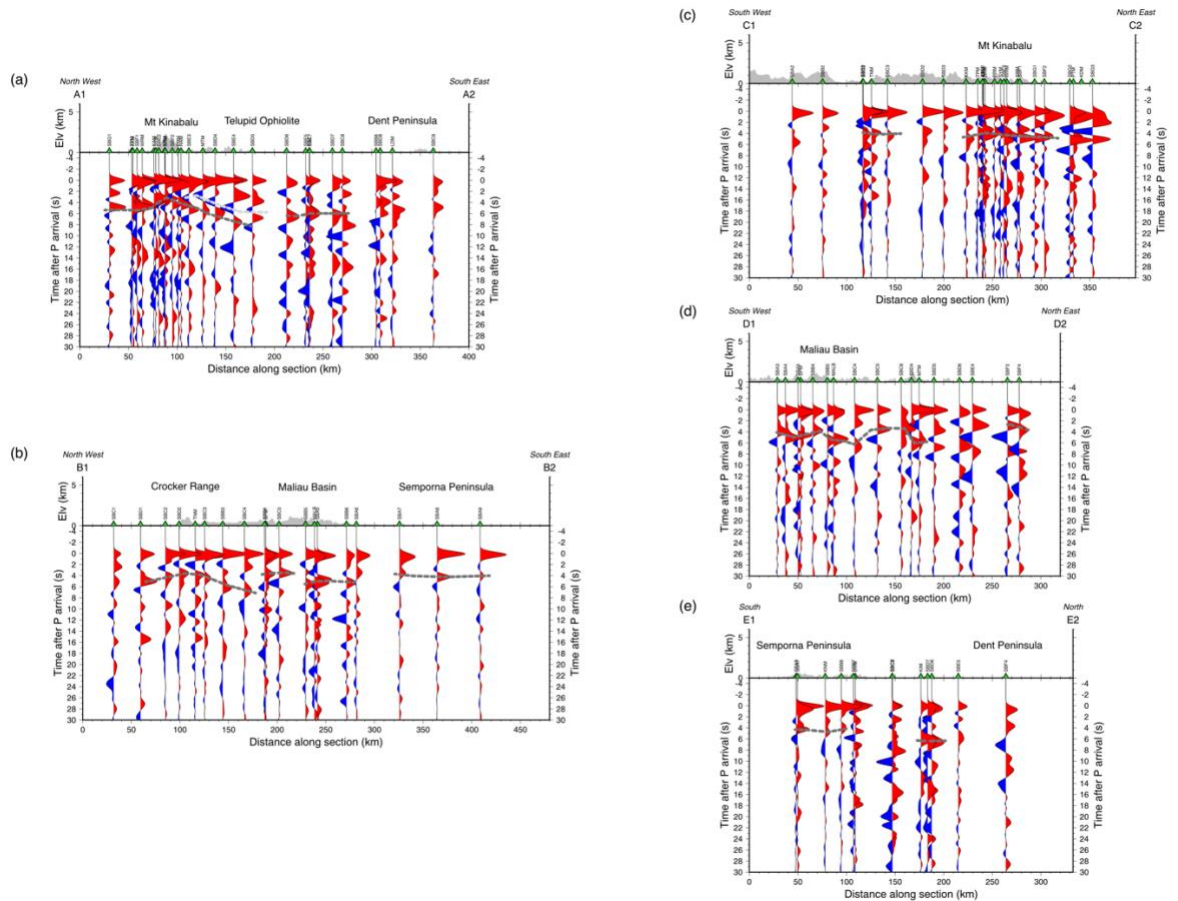
1032 **Figures**
1033
1034

1035
1036



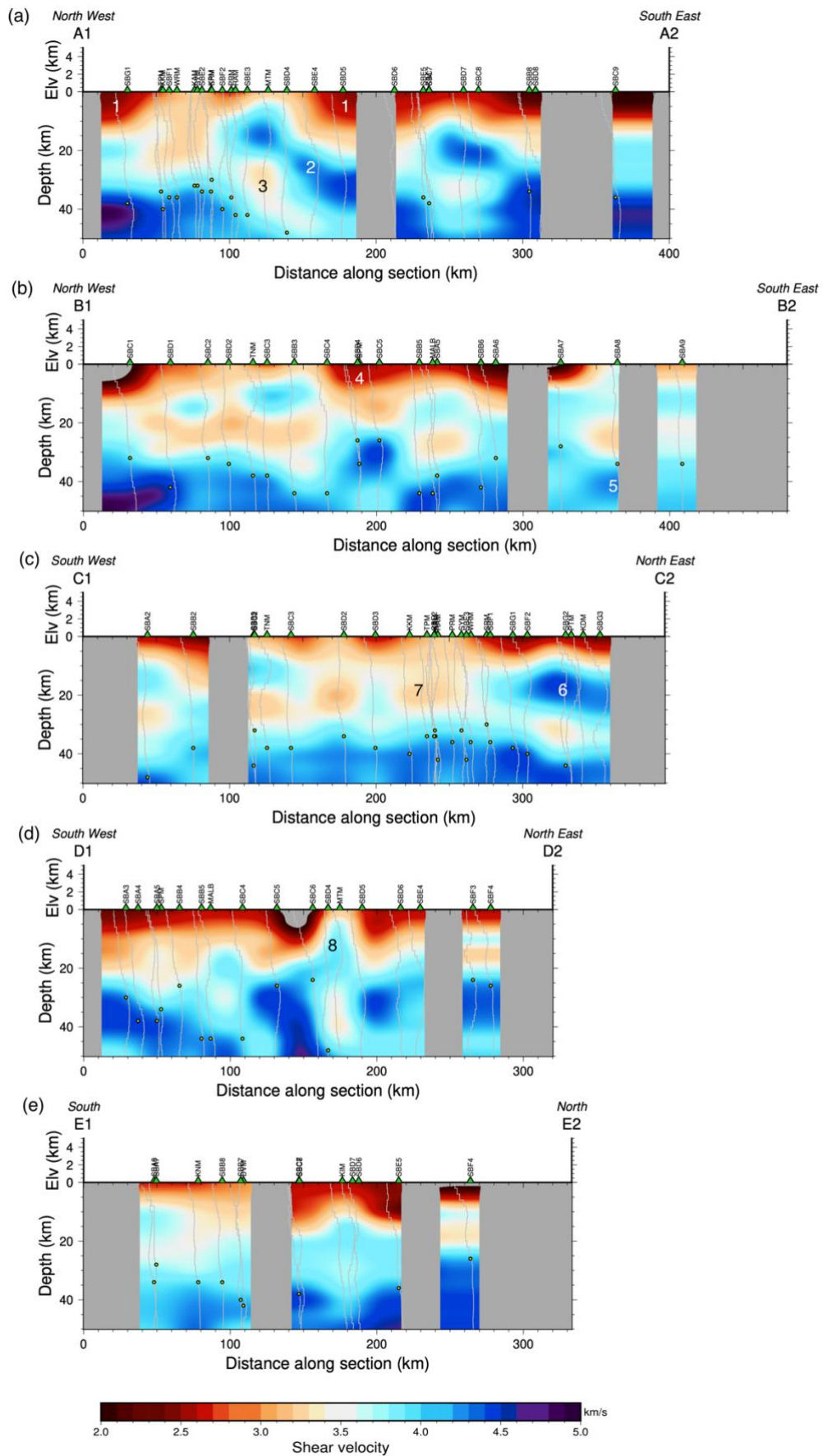
1037
1038
1039
1040
1041
1042
1043
1044
1045
1046
1047
1048
1049
1050
1051
1052
1053

Figure 1: Map of seismometer stations in Sabah used in this study. Blue triangles are MetMalaysia seismometers deployed before 2017, yellow triangles are MetMalaysia seismometers deployed after 2017. Pink (6TD) and Purple (3ESP) triangles are seismometers deployed as part of the nBOSS project. Lines of section are shown: A1-A2 (6.56°N 115.97°E - 4.78°N 119.09°E), B1-B2 (5.691°N 115.05°E - 3.82°N 118.96°E), C1-C2 (4.25°N 115.30°E - 7.26°N 117.23°E), D1-D2 (4.25°N 116.30°E - 6.67°N 117.88°E) E1-E2 (4°N 118°E - 7°N 118°E). Geological units are plotted after Hall (2013). The inset map shows the wider geographical area, with the area of the main map highlighted by the blue box, and plate boundaries after Bird (2003), are shown by red lines.

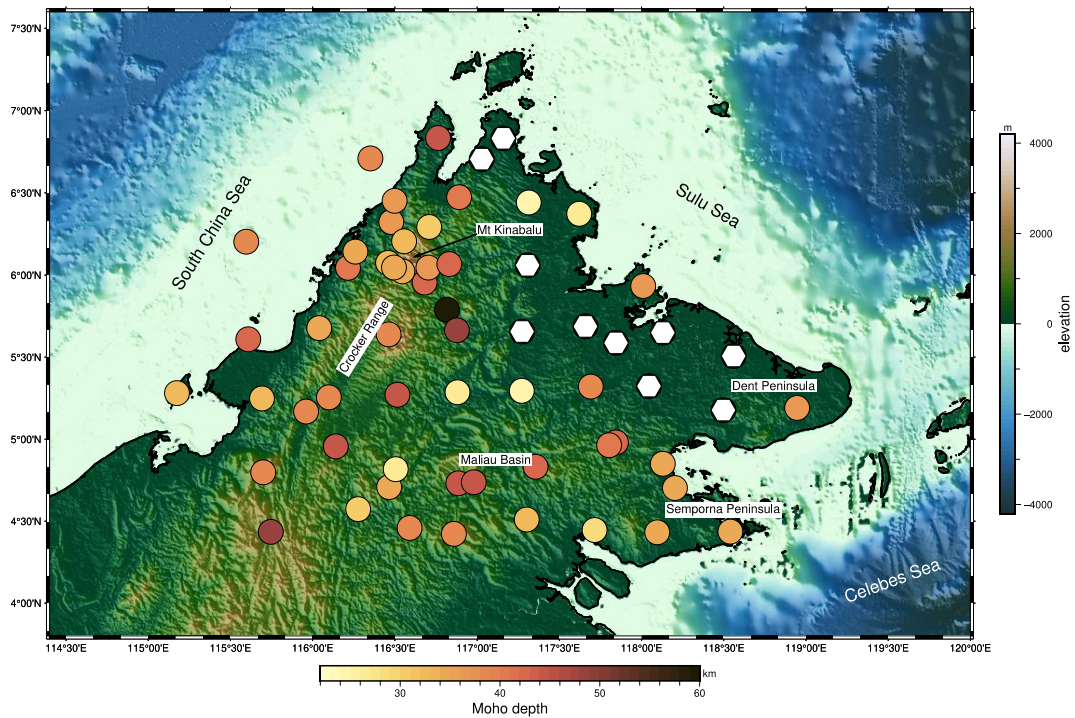


1054
1055

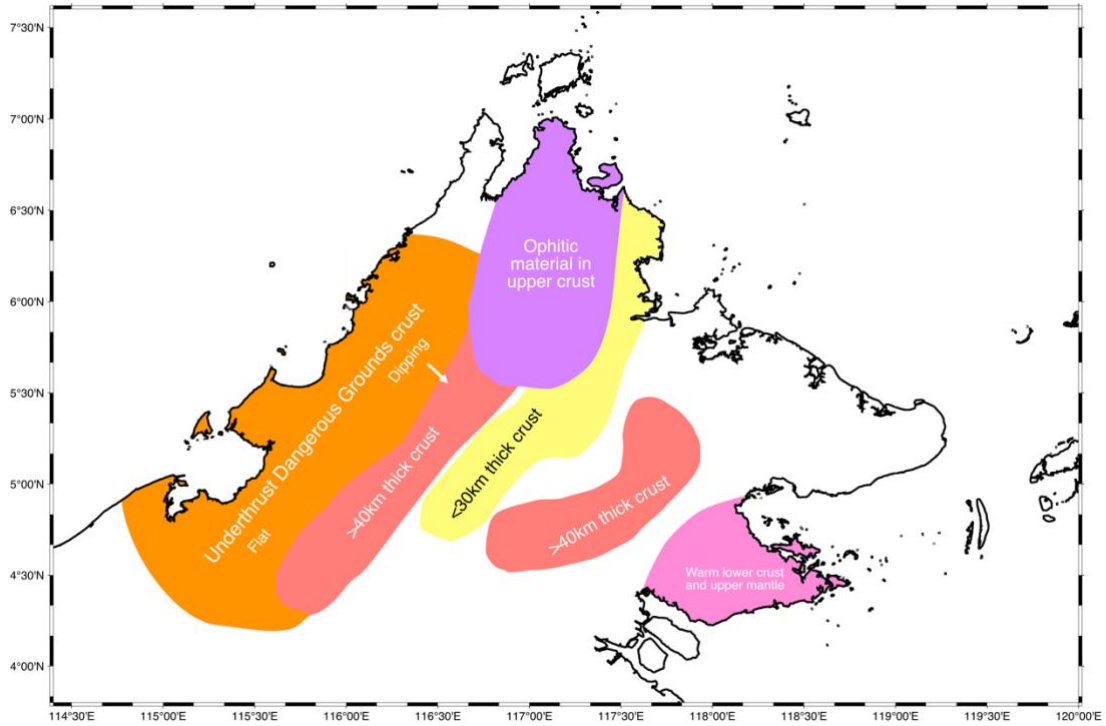
1056 **Figure 2:** Stacked receiver functions along the lines (a) A1-A2, (b) B1-B2, (c)
1057 C1-C2, (d) D1-D2, and (e) E1-E2. Positive arrivals are filled red, and negative
1058 arrivals are filled blue. In both cases receiver functions from stations within 50
1059 km of each line have been projected onto the section, along with their
1060 respective station (green triangles), and topography is plotted above. The
1061 dark grey dashed line highlights positive arrivals, likely from the P-to-S
1062 conversion at the Moho. The light grey dashed line highlights negative arrivals
1063 corresponding to a velocity increase with depth in the crust.



1065 **Figure 3:** Shear velocity vs depth along lines (a) A1-A2, (b) B1-B2, (c) C1-C2,
 1066 (d) D1-D2, (e) E1-E2 from the joint inversion of receiver function and surface
 1067 wave data. 1-D models from stations within 50 km of the line of section are
 1068 interpolated to make the cross-sections. Grey areas indicate areas with no
 1069 station coverage. Green triangles mark the location of stations. Topography
 1070 along the line of section is plotted above. Labelled velocity anomalies 1-8
 1071 are discussed in the text.
 1072
 1073



1074
 1075 **Figure 4:** Moho depths at seismometer stations in Sabah picked from 1D
 1076 shear velocity models from the joint inversion of receiver function and surface
 1077 wave data. The colour of the circle indicated Moho depth for the station
 1078 located at that point, as shown in the scale. White hexagons are locations
 1079 where there was no clear Moho to be picked or where there were multiple
 1080 plausible velocity discontinuities that could be the Moho.
 1081
 1082



1083
 1084
 1085
 1086
 1087
 1088
 1089
 1090
 1091
 1092
 1093
 1094
 1095
 1096
 1097
 1098
 1099
 1100
 1101
 1102
 1103
 1104
 1105
 1106
 1107
 1108
 1109
 1110
 1111
 1112

Figure 5: Summary map highlighting the key interpretations from this study from the shear velocity models derived from the joint inversion of receiver function and surface wave data.

1113 **Imaging subduction, collision, and extension in**
1114 **northern Borneo: Constraints from receiver**
1115 **functions**

1116
1117
1118
1119
1120
1121
1122
1123
1124
1125
1126
1127
1128
1129

Amy Gilligan(1),* David G. Cornwell(1), Nicholas Rawlinson(2), Felix Tongkul(3), Simone Pilia(4), Tim Greenfield(2), Conor Bacon(5)

1. *School of Geosciences, University of Aberdeen, Aberdeen, UK*
2. *Department of Earth Sciences, University of Cambridge, Cambridge, UK*
3. *Faculty of Science and Natural Resources, Universiti Malaysia Sabah, Kota Kinabalu, Malaysia*
4. *College of Petroleum Engineering and Geosciences, King Fahd University of Petroleum and Minerals, Dhahran, Saudi Arabia*
5. *Lamont-Doherty Earth Observatory, Columbia University, Palisades, New York, USA*

1130 * Corresponding author: amy.gilligan@abdn.ac.uk

1131
1132
1133
1134

Supplementary Material

1135 **Supplementary table 1:** The name, instrument type, and location of the
1136 seismometers used in this study, together with the number of good receiver
1137 functions after quality control, and the crustal thickness estimated from the
1138 joint inversion of receiver function and surface wave data. Where the crustal
1139 thickness is N/A this is because there were no good receiver functions for that
1140 station. Where crustal thickness is 'X' these are stations where it was not
1141 possible to estimate the crustal thickness from the velocity model.
1142

Network	Station	Instrument type	Latitude (N)	Longitude (E)	# of receiver functions	Crustal thickness (km)
YC	SBA2	3ESP	4.43506	115.74560	76	48
YC	SBA3	6TD	4.57347	116.27660	74	30
YC	SBA4	3ESP	4.45879	116.58977	73	38
YC	SBA5	6TD	4.42271	116.85881	84	38
YC	SBA6	3ESP	4.51025	117.30176	18	32
YC	SBA7	6TD	4.44587	117.71442	47	28
YC	SBA8	3ESP	4.43208	118.09522	183	34

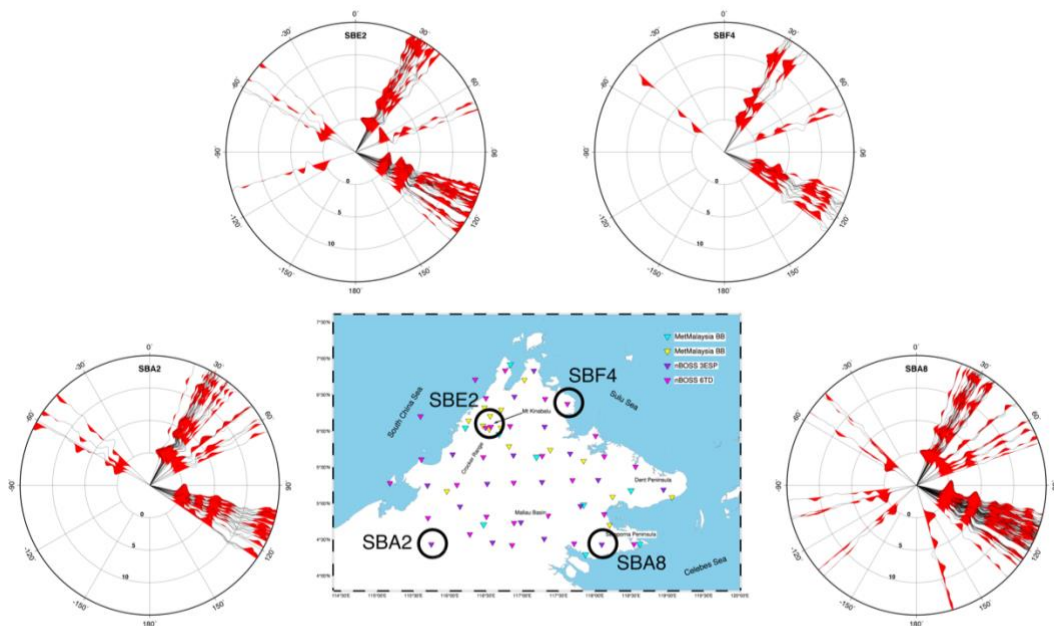
YC	SBA9	6TD	4.43637	118.53992	76	34
YC	SBB2	6TD	4.79788	115.69913	62	38
YC	SBB3	3ESP	4.95640	116.14096	126	44
YC	SBB4	6TD	4.81717	116.50497	36	26
YC	SBB5	6TD	4.73101	116.88574	82	44
YC	MALB	3ESP	4.73740	116.97997	51	44
YC	SBB6	6TD	4.83194	117.35575	54	42
YC	SBB7	3ESP	4.96355	117.80282	70	40
YC	SBB8	6TD	4.85014	118.12941	79	34
YC	SBC1	6TD	5.28108	115.17476	24	32
YC	SBC2	3ESP	5.24880	115.69165	114	32
YC	SBC3	6TD	5.25540	116.09856	48	38
YC	SBC4	3ESP	5.27107	116.51573	76	44
YC	SBC5	6TD	5.28637	116.88076	73	26
YC	SBC6	3ESP	5.29518	117.27165	19	24
YC	SBC7	6TD	5.32075	117.69134	23	42
YC	SBC8	3ESP	5.32373	118.04523	13	X
YC	SBC9	3ESP	5.19098	118.94610	54	36
YC	SBD1	6TD	5.60898	115.60830	42	42
YC	SBD2	3ESP	5.67735	116.03960	55	34
YC	SBD3	6TD	5.63900	116.46225	89	38
YC	SBD4	3ESP	5.66416	116.87691	86	48
YC	SBD5	6TD	5.65637	117.27355	28	X
YC	SBD6	3ESP	5.68750	117.65900	28	X
YC	SBD7	6TD	5.64967	118.12955	80	X
YC	SBD8	6TD	5.50699	118.56041	34	X

YC	SBE1	6TD	6.20282	115.5963	33	38
YC	SBE2	6TD	6.04611	116.49462	83	34
YC	KINA	6TD	6.05826	116.56593	0	N/A
YC	SBE3	6TD	6.06708	116.83097	63	42
YC	SBE4	3ESP	6.05975	117.30715	48	X
YC	SBE5	6TD	5.93328	118.01012	37	36
YC	SBF1	6TD	6.45216	116.49845	48	36
YC	SBF2	3ESP	6.47376	116.89069	42	40
YC	SBF3	6TD	6.44177	117.31431	95	24
YC	SBF4	6TD	6.37312	117.62083	30	26
YC	SBG1	6TD	6.70950	116.35092	22	38
YC	SBG2	6TD	6.83352	116.76262	49	44
YC	SBG3	3ESP	6.83170	117.15904	55	X
MY	DVM	STS-2.5	4.98038	117.84421	11	42
MY	FSM	STS-2.5	5.0855	119.0627	0	N/A
MY	KAM	STS-2.5	6.0745	116.4583	45	32
MY	KDM	SS-1 Ranger	6.9167	116.8333	0	N/A
MY	KIM	STS-2.5	5.587083	117.844717	48	X
MY	KKM	STS-2	6.0443	116.2147	61	40
MY	KNM	STS-2.5	4.7026	118.203	82	34
MY	KPM	STS-2.5	6.0227	116.545417	21	34
MY	LDM	STS-2.5	5.1777	118.498	35	X
MY	MTM	STS-2.5	5.789333	116.81665	37	60
MY	PRM	STS-2.5	6.0455	116.70375	51	36
MY	PTM	STS-2.5	6.70523	117.0283	39	X

MY	RAM	STS-2.5	5.9546	116.681	64	42
MY	SDM	SS-1 Ranger	5.6409	117.195	0	N/A
MY	SGM	STS-2.5	5.0912	118.2446	0	N/A
MY	SMM	SS1- Ranger	4.439838	118.622028	0	N/A
MY	SPM	STS-2	4.7083	116.465	9	34
MY	SRM	STS-2.5	6.29265	116.708383	36	30
MY	SYM	STS-2.5	6.20585	116.5559	42	32
MY	TLM	STS-2.5	5.7391	117.385	0	N/A
MY	TNM	STS-2.5	5.168633	115.960183	27	38
MY	TPM	STS-2.5	6.1427	116.2596	19	34
MY	TSM	SS-1 Ranger	4.2936	117.8725	0	N/A
MY	WRM	STS-2.5	6.3229	116.47825	29	36

1143

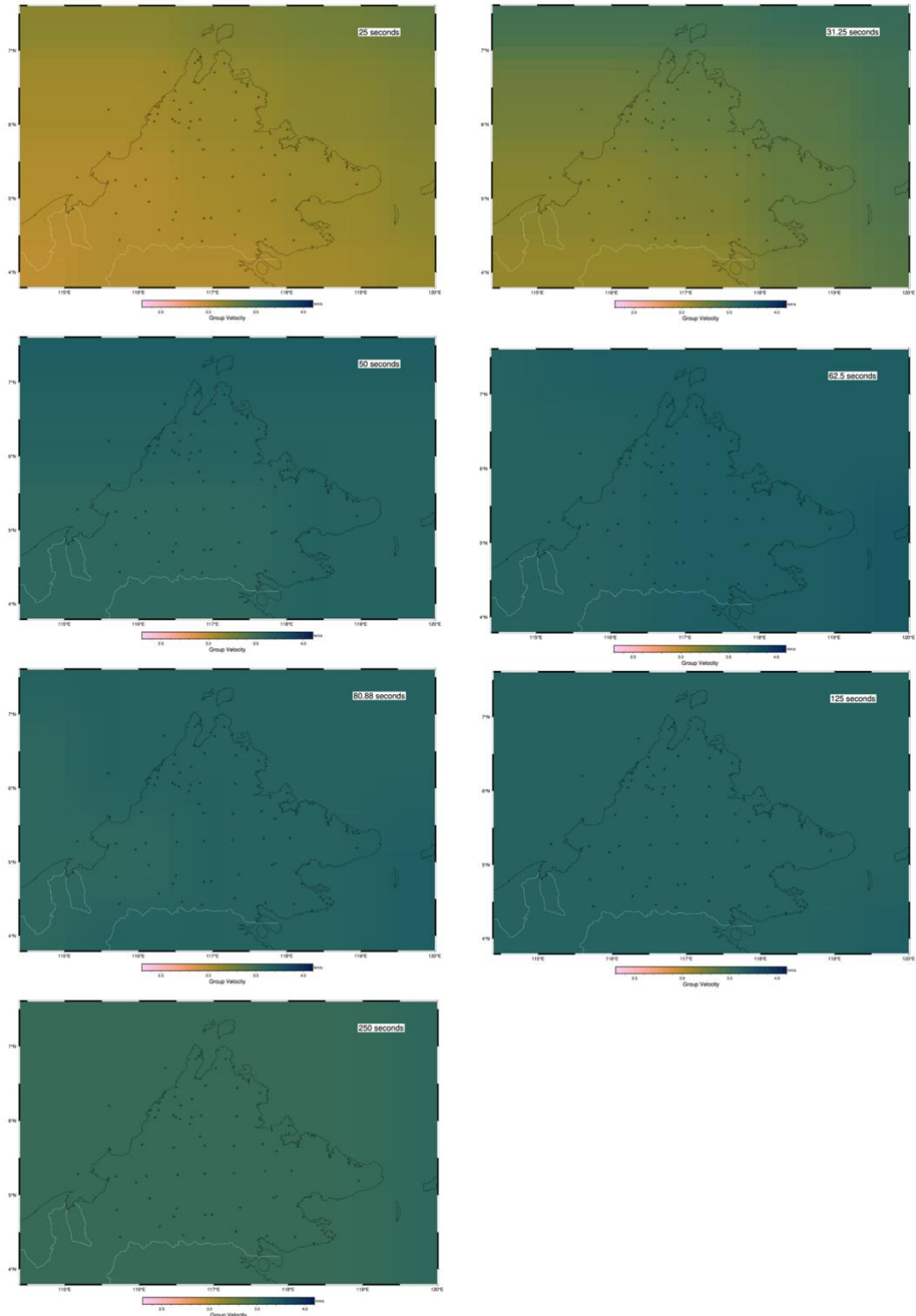
1144



1145

1146 **Supplementary figure 1:** Examples of the receiver functions of individual
1147 events used in the station stacks for four stations across Sabah: SBA2,
1148 SBE2, SBF4, and SBA9, and a map indicating the station locations. Receiver
1149 functions are plotted with respect to backazimuth with positive amplitudes
1150 filled red.

1151



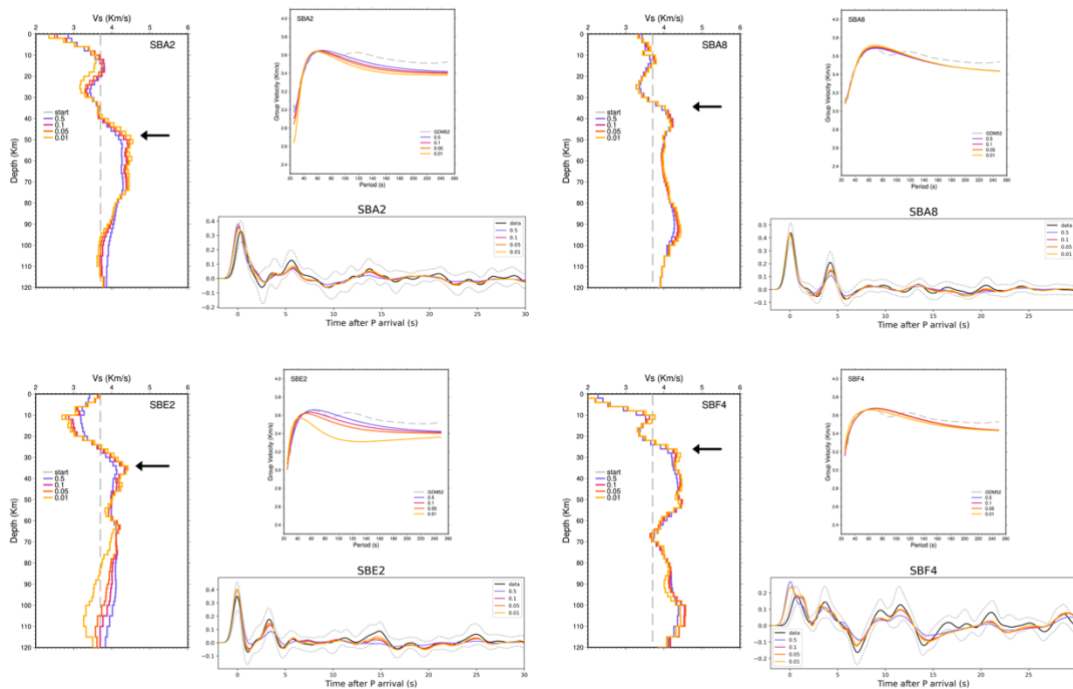
1152

1153

1154 **Supplementary figure 2:** Group velocity maps for the GDM52 model
1155 (Ekstrom, 2011), for the periods 25s, 31.25s, 50s, 62.5s, 80.88s, 125s, and
1156 250s.

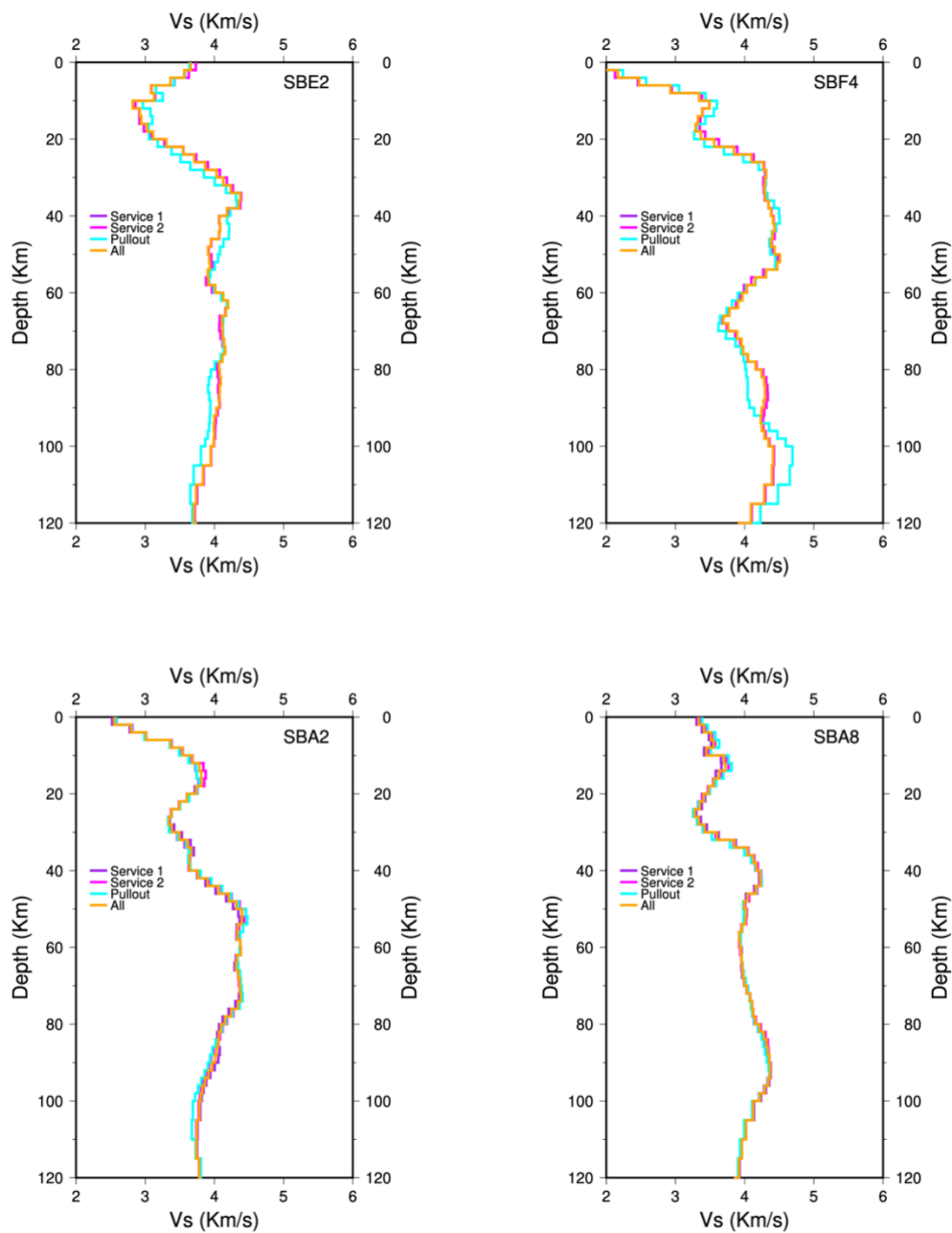
1157

1158



1159

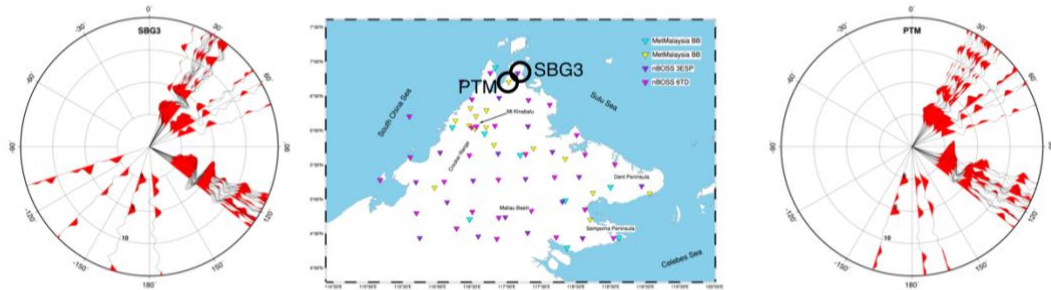
1160 **Supplementary figure 3:** Examples of models of shear velocity vs depth from
1161 the joint inversion of surface wave and receiver function data, and the receiver
1162 functions for these models for four stations across Sabah: SBA2, SBE2,
1163 SBF4, and SBA9. On each of the shear velocity and receiver function plots the
1164 coloured lines show the results from testing different weights of receiver
1165 function and surface wave data. On the shear velocity plots, the black arrow
1166 indicates the depth that is picked for the Moho in each example. On the
1167 receiver function plots, the receiver function data are shown in black.
1168



1169
 1170
 1171
 1172
 1173
 1174
 1175
 1176
 1177

Supplementary figure 4: Examples of models of shear velocity vs depth from the joint inversion of surface wave and receiver function data four stations SBA2, SBE2, SBF4, and SBA9 with a p value of 0.1. On each shear velocity model the coloured lines show the different models that result from testing different subsets of the receiver function data: Service 1 (purple) is from the inversion of stacked receiver functions for events between March 2018-Sept 2018, Service 2 (magenta) is from the inversion of stacked receiver functions from events between Sept 2018-March 2019, Pullout is from the inversion of

1178 stacked receiver functions from events between March 2019-Jan 2020, and
1179 All is from the inversion of stacked receiver functions for the whole time
1180 period, as shown in Supplementary figure 1. For each station, the same
1181 surface wave dispersion data was used for each of the inversions.
1182
1183



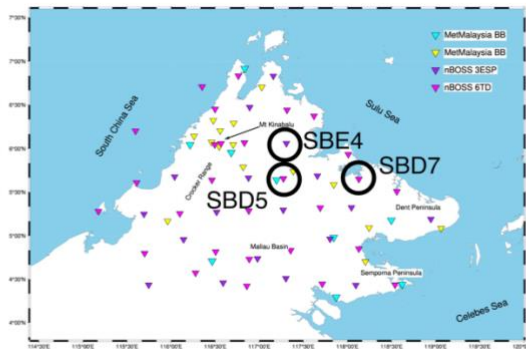
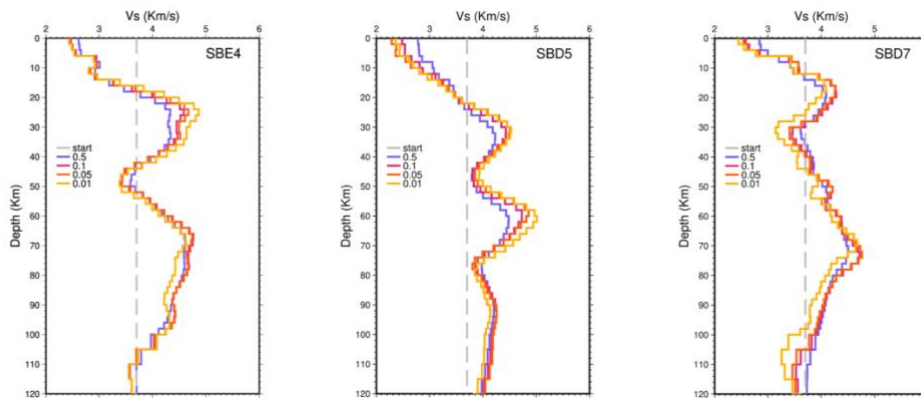
1184
1185 **Supplementary figure 5:** Examples of the receiver functions of individual
1186 events used in the station stacks for SBG3 (left) and PTM (right) and a map
1187 indicating the station locations. Receiver functions are plotted with respect to
1188 backazimuth with positive amplitudes filled red.

1189

1190

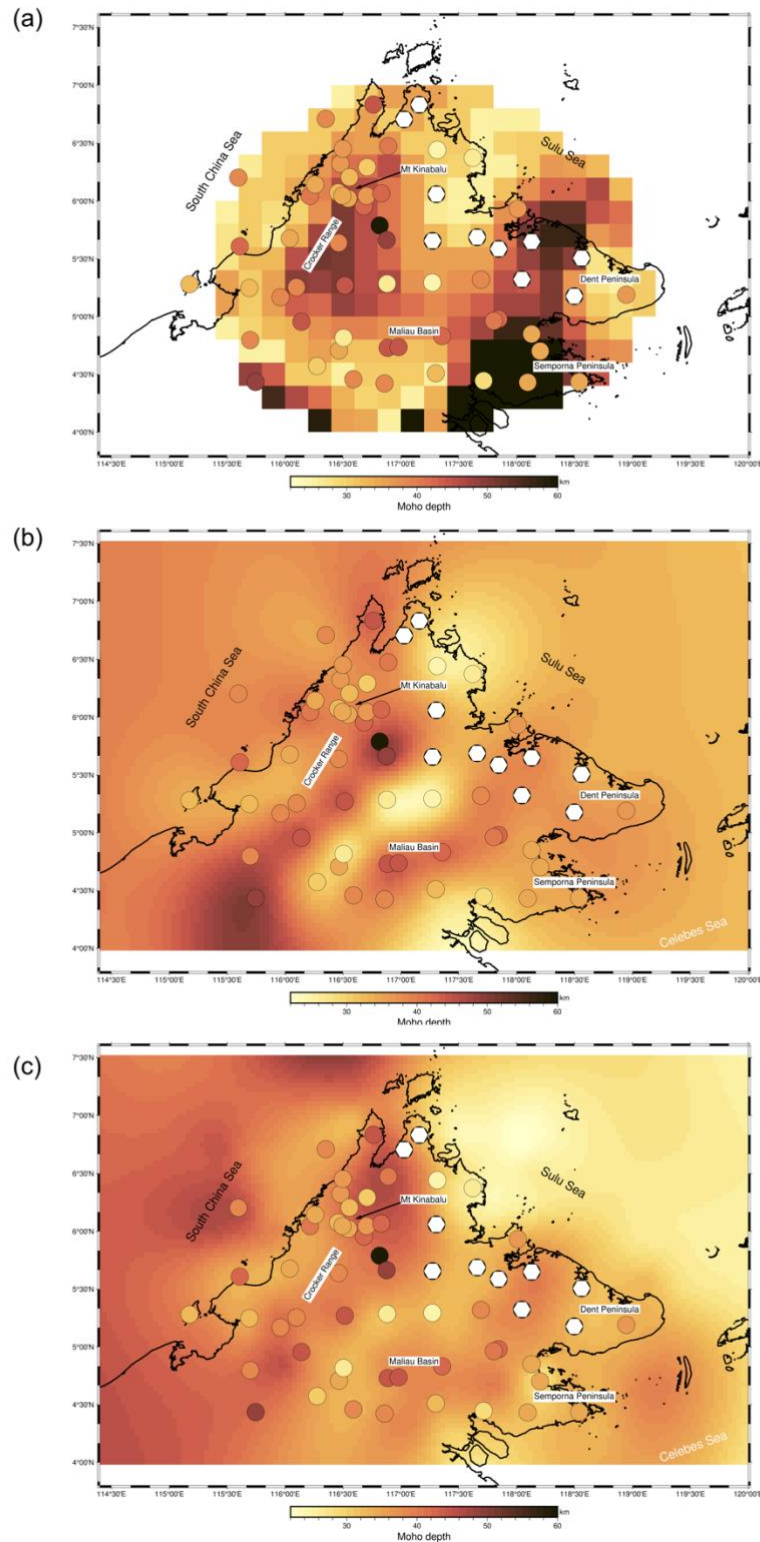
1191

1192



1193
 1194
 1195
 1196
 1197
 1198
 1199
 1200
 1201
 1202
 1203
 1204

Supplementary figure 6: Examples of models of shear velocity vs depth from the joint inversion of surface wave and receiver function data for stations where a Moho was challenging to identify in this study. SBE4 and SBD5 are examples of stations with two potential discontinuities, while SBD7 shows a gradual increase in velocities over a wide depth range. On each shear velocity model the coloured lines show the different models that result from testing different weights of receiver function and surface wave data.



1205
 1206
 1207
 1208
 1209
 1210
 1211
 1212

Supplementary figure 7: Comparison of Moho depths from this study (circles) with other Moho depth estimates from other studies of the region. (a) comparison with the Moho depth from Greenfield et al., (2022) based on the 4.1km/s velocity contour in their shear velocity model, (b) comparison with the Moho depth from Linang et al, (2022) from the interpolation of crustal depths obtained from stacked VDSS traces, assuming the depths reflect the Moho beneath stations, (c) comparison with the Moho depth from Linang et al,

1213 (2022) from the interpolation of crustal depths at reflection points in the VDSS
1214 method.
1215

1216

1217
1218